Simple and double microemulsions via the capillary breakup of highly stretched liquid jets

A. Evangelio, F. Campo-Cortés and J.M. Gordillo†

Área de Mecánica de Fluidos, Departamento de Ingenería Aeroespacial y Mecánica de Fluidos, Universidad de Sevilla, Avenida de los Descubrimientos s/n 41092, Sevilla, Spain.

(Received ?? and in revised form ??)

We present an exhaustive experimental and theoretical study on the shapes of the type of jets, simple or compound, formed as a consequence of the injection of either one or two immiscible liquids within a co-flow of another liquid whose viscosity can be chosen so that the characteristic outer stream Reynolds number, Re_o, can be varied in a wide range of values. Our slender body theory in Gordillo *et al.* (2014) is extended to predict the shapes of simple jets when Re_o is such that $Re_o \gg 1$ and also to predict the shapes of compound jets in the case of $Re_o \lesssim O(1)$. The validity of our theoretical results, applicable to describe the dynamics of simple or compound jets within an outer carrier fluid in a wide variety of practical situations, is tested using a setup where the liquids flow from a pressurized chamber towards an extraction tube, finding a very good agreement between the predicted and the observed shapes. Moreover, when $Re_o \lesssim O(1)$ and thanks to the fact that the liquid jets produced using our method are highly stretched in the downstream direction, we find that the values of the critical capillary number above which a steady stretched jet is produced, with the capillary number defined here using the outer stream velocity and viscosity, is well below the corresponding critical values characterizing other similar procedures, like flow-focusing. This experimental result, which is supported by a spatio-temporal stability analysis in which the axial gradients of the unperturbed solution are retained in the dispersion relation, imply a substantial saving of energy and of the volume of outer liquid necessary to generate a steady capillary jet from which drops are regularly produced. Additionally, making use of continuity arguments and of the fact that drops are formed as a consequence of the growth of a capillary instability, we provide closed expressions for the drop diameters and their production frequencies when the capillary number is above the critical one, in very good agreement with experiments. The simple or double microemulsions generated by the capillary disintegration of the type of simple or compound highly stretched steady jets described here, might find applications in biotechnology, pharmacy, cosmetics or material science.

1. Introduction

The number of recent contributions aimed at describing the disintegration of liquid jets *in air* is a natural consequence of the relevance of drop and fiber generation processes in many different technological applications such as ink-jet printing, catalysis, atomization or combustion (Basaran *et al.* 2013; Loscertales *et al.* 2004; Eggers & Villermaux 2008). New biotechnological, pharmaceutical, medical or environmental applications demand, however, the controlled generation of micron-sized simple or compound drops *within another immiscible liquid* for their use as biological microreactors, as drug carriers (Barrero

† Email address for correspondence: jgordill@us.es

& Loscertales 2007), or as building blocks of new materials (Fernández-Nieves *et al.* (2007) and Lopez-Leon *et al.* (2011)). In conventional emulsification methods, the uncontrolled fluctuating shear stresses created by either mechanical agitation or by the turbulent flow of the continuous phase (Garti (1997) and Rodríguez-Rodríguez *et al.* (2006)), lead to the formation of emulsions consisting of simple or compound drops with a large size dispersion (Chong *et al.* 2015). New applications require, however, the generation of monodisperse simple or complex emulsions composed of drops of controllable diameters (Shah *et al.* (2008) and Zarzar *et al.* (2015)), and it is our purpose here to provide a detailed experimental and theoretical description on the generation of simple and compound jets and drops within another immiscible liquid under well controlled and realistic operating conditions.

The capability of microfluidics to produce drops of controllable size (Thorsen *et al.* 2001), has triggered the emergence of a myriad of different emulsification techniques with different geometrical arrangements but based on very similar physical principles. A few of these techniques rely on the use of electrical stresses to stretch and accelerate a stream of a conducting liquid for its subsequent disintegration into droplets in air (see, e.g. de la Mora (2007) and Collins *et al.* (2013)) and within an insulator liquid bath (see, e.g. Loscertales *et al.* (2002) and Marín *et al.* (2007)). Nevertheless, most of the new emulsification methods make use of stresses of hydrodynamical origin to force the production of droplets in PDMS microchannels. For instance, in Garstecki *et al.* (2006), monodisperse simple microemulsions are generated by means of a crossflow at the junction of two perpendicular microchannels whereas Anna *et al.* (2003), reports the generation of micron-sized drops using a two–dimensional flow-focusing type of geometry. Simple and double monodisperse emulsions composed of drops of controllable size can also be produced in glass capillaries, as it was originally reported by Utada *et al.* (2007) and Utada *et al.* (2005) and, more recently, by Oh *et al.* (2006) and Nabavi *et al.* (2015). A common feature of all the methods enumerated above is that the high production frequencies usually needed in applications, require the production of drops in the so called jetting regime, i.e., drops form as a result of the growth of capillary instabilities convected downstream either simple or compound microjets flowing within an immiscible carrier liquid (Utada *et al.* (2008) and Herrada *et al.* (2010)).

The capillary stability of a cylindrical liquid jet immersed into another immiscible liquid, was previously studied by Tomotika (1935), whereas the stability analysis corresponding to the analogous case of compound liquid jets, was performed by Sanz & Meseguer (1985) and Chauhan *et al.* (2000). Chauhan *et al.* (2000) reported the existence of two different unstable capillary modes and showed that, under a vast majority of conditions, the growth rate of the mode for which the two interfaces grow in phase, is larger than the corresponding growth rate of the mode where the two interfaces grow out of phase. This finding, which was later on confirmed by means of non linear numerical simulations by Suryo *et al.* (2006) and Vu *et al.* (2013), indicates that most system conditions promote the generation of compound drops, a result in accordance with the experimental fact that the capillary breakup of a compound jet within another immiscible liquid constitutes a feasible and practical method for the controlled generation of double emulsions. Moreover, Chauhan *et al.* (2000) also found that the differences between the growth rates of the two different unstable modes identified, become even larger for decreasing thicknesses of the annulus surrounding the inner jet. Interestingly enough, Chauhan *et al.* (2000) also reported that, in the limit of thin liquid annuli, the compound jet behaves as a single jet with the interfacial tension coefficient resulting from the addition of the two tensions.

As it is pointed out above, many different microfluidic devices have been designed with

the purpose of generating, in a controlled manner, simple or double microemulsions at production frequencies exceeding 5 kHz by means of the capillary breakup of simple or compound jets flowing into another immiscible liquid. However, the progress made on the experimental (Hertz & Hermanrud 1983) and analytical description of the dynamics of such type of microjets are still far from being comparable to the advances accomplished in the analysis of the analogous case of liquid jets in air (García & Castellanos 1994; Eggers & Dupont 1994; Guerrero *et al.* 2012; Rubio-Rubio *et al.* 2013; Ambravaneswaran *et al.* 2004; Driessen *et al.* 2014). Motivated by the potential applications of simple and double microemulsions, in this contribution we will analyze, both from an experimental and theoretical point of views, the dynamics of long liquid jets breaking into droplets of very similar size within an outer stream of another immiscible liquid. More precisely, it is our purpose here to extend the analytical framework developed in Castro-Hernández *et al.* (2012) and Gordillo *et al.* (2014) to describe the generation and subsequent breakup of simple jets when the Reynolds number characterizing the outer flow of liquid is much larger than unity. We will also extend our previous slender body theory, valid in the Stokes limit, to analyze the dynamics of compound jets under creeping flow conditions. Our analytical results will be checked by comparing the computed shapes with those observed experimentally in a type of setup, already described in Evangelio *et al.* (2015) and also sketched in figure 1, which shares similarities with both the flow focusing and the selective withdrawal geometries (Gañán Calvo (1998) and Cohen *et al.* (2001)). Our technique, which will be termed as *confined selective withdrawal*, allows controlling the flow rates of the different liquids with high precision and, most importantly, to visualize the resulting simple or compound jet in a straightforward manner thanks to the fact that the tubes used in our design are millimetric. Our procedure is conceptually similar to that in Barrero & Loscertales (2007) and Marín *et al.* (2007), where two immiscible fluids issued from two coaxial tubes are stretched by electrical stresses, being the only conceptual difference that, in our case, electrical stresses are substituted by those of hydrodynamic origin. We will focus on the generation of simple and compound drops arising from the capillary breakup of *surfactant-free* simple or compound stretched microjets (Suryo & Basaran (2006) and Anna (2016)).

The paper is structured as follows: in §2, we present the phenomenological description of the jet and drop formation processes under those conditions for which the Reynolds number characterizing the outer coflow, Re_o, is either large or of order unity or smaller. In §3, we develop a slender-body approximation to predict the steady shapes of the liquid jets in both the high and low Reynolds number limits; in this section, a comparison with experiments is also provided. In §4 scalings for the drop formation frequencies and drop diameters are deduced and compared with experiments. In §5 we determine the values of the critical capillary numbers for steady jets to be formed in the low Reynolds number limit. The main results of the paper are summarized in §6.

2. Phenomenology

In our experimental setup, sketched in figure 1, a flow rate Q_o of an outer liquid of density ρ_o and viscosity μ_o, constituting the continuous phase, flows into a chamber of pressure P_0 larger than the atmospheric one, P_a. The fluid(s) to be dispersed enter within the reservoir through either a cylindrical tube of inner diameter D_i or through two coaxial tubes of respective inner diameters D_i and D_m. In the case of generation of simple emulsions, the density, viscosity and the flow rate of the liquid to be dispersed will be denoted, in what follows, as ρ_i, μ_i and Q_i. Analogously, $\rho_{i,m}$, $\mu_{i,m}$ and $Q_{i,m}$ will indicate the material properties and the flow rates of the inner(i)/middle(m) liquids contained in

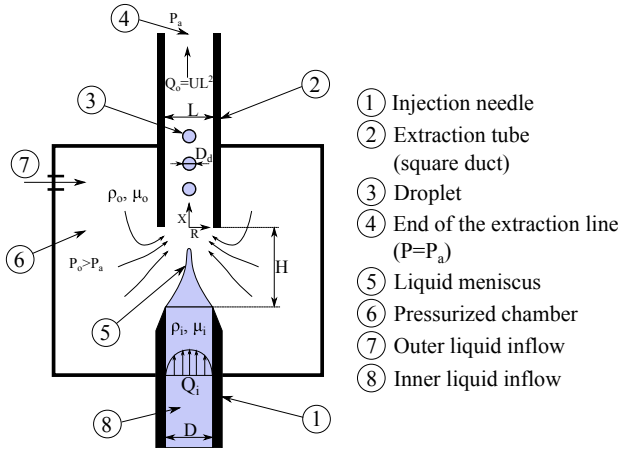

Figure 1: Sketch of the drop production device operating in the regime of interest for applications, in which drops with very similar diameters D_d are produced. Drops are regularly emitted from the tip of a steady and highly stretched liquid ligament attached at the exit of the injection needle. The origin of the dimensionless coordinate $x = X/L$ is located at the entrance of the square duct. The imposed inner liquid flow rate is Q_i and the outer liquid flow rate is UL^2.

the drops forming the double emulsion (see figure 2). The different liquids involved in the emulsification process flow from the pressurized reservoir towards the atmosphere through a square extraction tube of width $L = 1$ mm, aligned with the injection tube(s). In our device, the distance H separating the exit of the injection tube(s) from the entrance of the extraction tube is not fixed, but can be varied in a range of values. In the case of simple emulsions, the diameter D_i of the injection tube is also varied in the experimental study, but $D_i = 1000$ μm and $D_m = 1200$ μm remain fixed in the case of generation of complex emulsions. The imposed pressure difference $P_0 - P_a$ fixes the mean liquid velocity U in the square tube and also generates a pressure gradient from the exit of the injection tube(s) towards the entrance of the extraction duct, favoring the downstream stretching of the simple or compound liquid ligament. The outer liquid flow rate, $Q_o = UL^2$, is calculated by measuring the volume of liquid exiting the pressurized chamber in a given interval of time, whereas the flow rates Q_i and Q_m are controlled using syringe pumps. Images are captured using a Phantom V7 high speed camera which, depending on U, is operated between 1000 and 19000 frames per second. Table 1 shows the material properties of the different fluids used in the experiments as well as the values of the interfacial tension coefficients corresponding to the different liquid combinations investigated.

Due to the fact that $|\Delta\rho|gH/(32\mu_o U/L) \ll 1$ and $|\Delta\rho|gH/(\rho_o U^2) \ll 1$ with $\Delta\rho = \rho_i - \rho_o$, the experimental data to be presented in this section is not affected, in a first approximation, by buoyancy effects.

The experimental study is divided in two parts: the generation of simple emulsions within an outer liquid stream with a characteristic Reynolds number that can be set to values either much larger or much smaller than unity, and the generation of double emulsions in a co-flow of a liquid stream dominated by viscosity.

2.1. *Simple emulsions*

Figure 3 shows the generation process of an oil in water emulsion (O/W) by means of the capillary disintegration of a silicone oil jet of diameter $2R_j(X)$ flowing within a

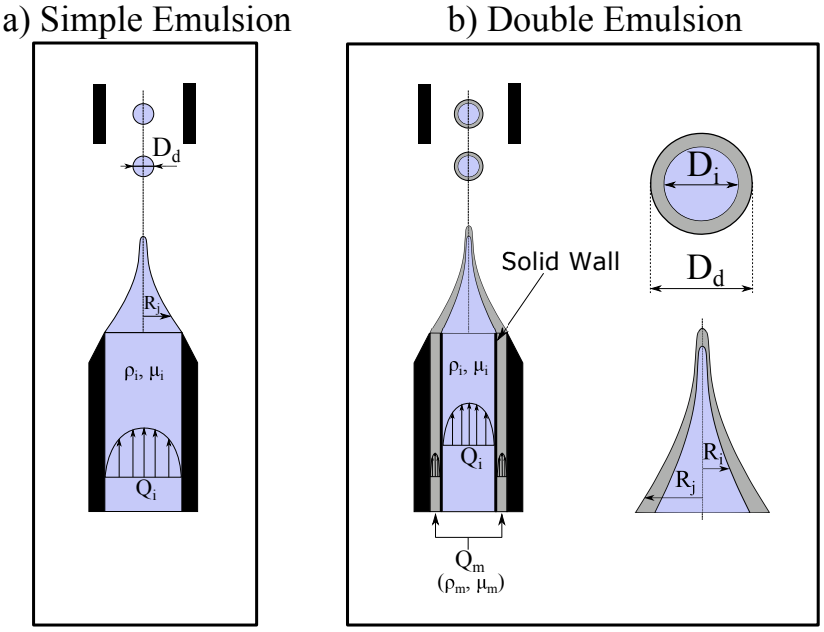

Figure 2: (a) Sketch illustrating the generation of simple emulsions. (b) In the case of double emulsions, two liquids with respective flow rates Q_i (inner liquid) and Q_m (middle liquid) are injected into the pressurized reservoir from a coaxial injection tube.

	Liquid	ρ (kg/m^3)	μ (cP)
(a)	Water	1000	1.0
(b)	Silicone Oil	930	5
(c)	Silicone Oil	930	10
(d)	Silicone Oil	967	100
(e)	Silicone Oil	970	1000
(f)	Propylene Glycol	1036	42
(g)	Glycerine (85%) + Water (15%)	1200	100
(h)	Glycerine (95%) + Water (5%)	1200	400
(i)	Glycerine (98%) + Water (2%)	1200	700

Table 1: Physical properties of the different liquids used in the experiments. The values of the interfacial tension coefficients for the different combinations of immiscible liquids used in the experimental study, are the following: Water - Silicone Oil, $\sigma = 0.04\,\mathrm{N\,m^{-1}}$. Propylene Glycol - Silicone Oil, $\sigma = 0.01\,\mathrm{N\,m^{-1}}$. Glycerine + Water - Silicone Oil, $\sigma = 0.03\,\mathrm{N\,m^{-1}}$. In (g), (h) and (i) mass percentages are used. The material properties of the different liquids used in this study have been obtained from the literature.

water stream of mean velocity U (see also the sketch in figure 1). Due to the fact that $Q_i \ll U\,L^2$, the liquid jet stretches in the downstream direction and, since $R_j \ll L$, the diameters of the droplets generated, D_d, are also sensibly smaller than the width of the extraction tube i.e., $D_d \ll L$. The Reynolds and Weber numbers characterizing the outer

flow of liquid

$$Re_o = \frac{\rho_o U\, L}{\mu_o}\,, \quad We_o = \frac{\rho_o U^2\,(Q_i/U)^{1/2}}{\sigma} \tag{2.1}$$

with $(Q_i/U)^{1/2}$ the characteristic diameter of the jet are, under all experimental conditions of interest for applications in which the continuous phase is water, such that $Re_o \sim O(10^3)$ and $We_o \gtrsim O(1)$. Indeed, although not shown here, for values of the Weber number below a threshold value of order unity, a long liquid jet is never formed. Instead, unequal-sized oil droplets of diameters comparable to D_i are formed at low frequencies right at the injection tube, in agreement with the findings reported in Utada *et al.* (2007). From the analysis of the images in figure 3a it can be inferred that, although the overall shape of the jets formed depend on the particular values of H and D_i, both the diameter of the jet right upstream the position where it breaks into drops and D_d, are not sensitive to geometrical modifications. Interestingly, figure 3b shows that the jet diameter at the position where it breaks into drops and D_d, can be reduced either by decreasing Q_i while keeping U constant or by increasing U for a given value of Q_i. Figure 3c shows that a two-fold increase of liquid viscosity, does not have an appreciable effect neither on the overall shape of the jets nor on the diameters of the droplets generated. From the images depicted in figure 3, notice that the liquid jet is not perfectly aligned with the axis of the extraction tube. This is due to the fact that for the values of the Reynolds number characterizing the outer liquid stream $Re_o \sim 1000$, the flow is prone to develop Kelvin-Helmholtz instabilities. In addition, $Re_o \sim 1000$ is close to the critical value for the laminar-turbulent transition of the flow in the extraction tube.

Figure 4 shows the generation of water in oil emulsions (W/O) by means of the capillary disintegration of a water jet flowing within an outer stream of a silicone oil with a viscosity of either $\mu_o = 100$ cP or $\mu_o = 1000$ cP and $Q_i \ll U\,L^2$. Similarly to the case of O/W emulsions illustrated in figure 3, the overall shape of the jet is sensitive to variations of D_i and H while the diameters of the droplets generated can be reduced/increased by varying Q_i and U. However, in this case, the stretched liquid jet is aligned with the axis of the extraction tube and, moreover, the drop production process is remarkably periodic: indeed, notice from the images in figure 4 that the diameters of the drops formed as well as the distances between two neighboring drops, is constant for fixed values of Q_i and U. Figure 4c shows that, in the present case, the diameters of the drops and the distances between them is sensitive to modifications of the outer liquid viscosity. The differences observed with the process of generation of O/W emulsions depicted in figure 3 are due to the fact that, in the case of figure 4, the characteristic Reynolds number is such that $Re_o \lesssim O(1)$. Moreover, in this case, the outer capillary number, defined as

$$Ca_o = \frac{\mu_o U}{\sigma}\,, \tag{2.2}$$

is above a threshold value $Ca^* \sim O(1)$ below which the frequency of drop production is not constant and, consequently, the diameters of the droplets composing the emulsion, are not uniform (Gordillo *et al.* 2014).

2.2. *Double emulsions*

Figure 5 shows the generation of double emulsions consisting of drops containing two immiscible liquids, the inner one is silicone oil and the middle is either propylene glycol or a glycerine-water mixture. The middle liquid is immiscible with the continuous phase which, in all the cases considered, is a silicone oil of viscosity $\mu_o = 1000$ cP. The process of generation of the double emulsion also resorts on the capillary breakup of a compound

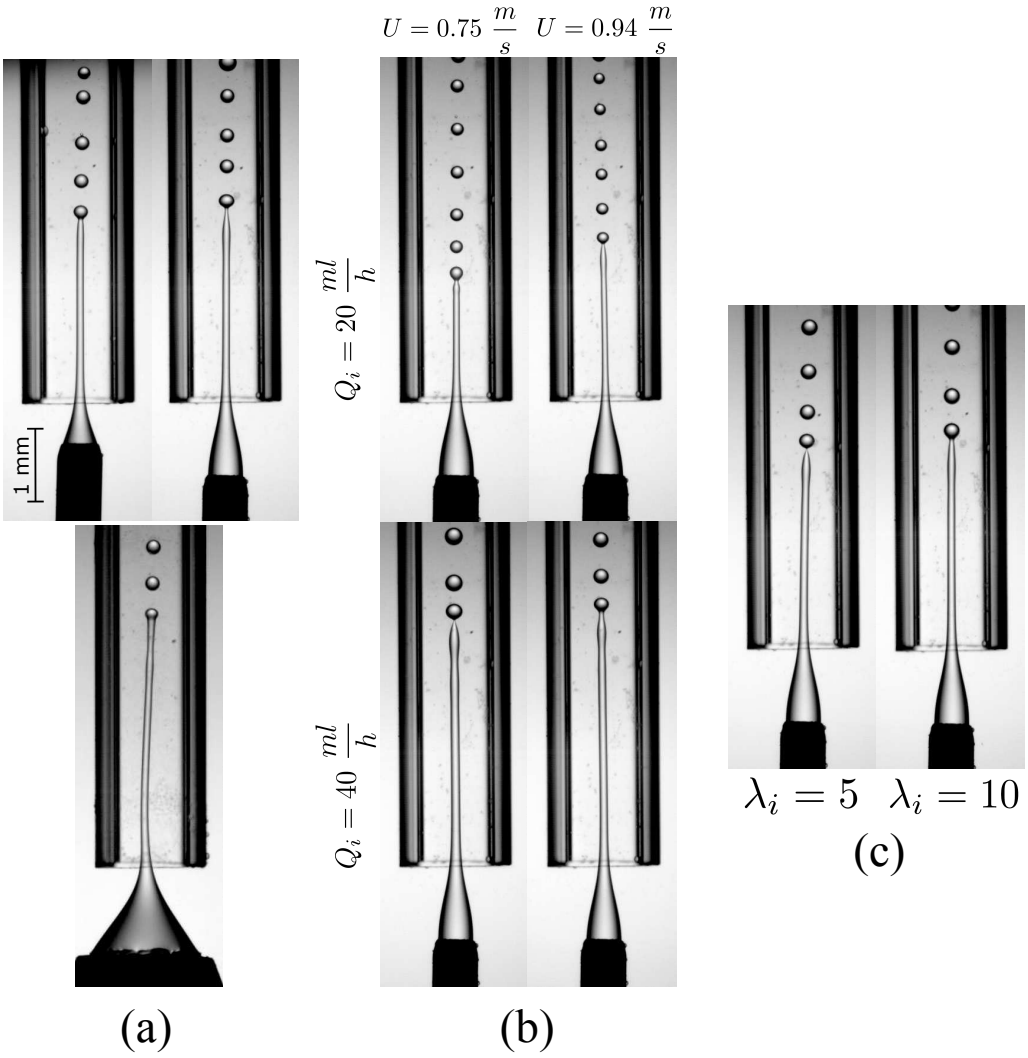

Figure 3: This figure shows the effect of varying the different parameters governing the generation of oil in water simple emulsions ($\sigma = 0.04\,\mathrm{N\,m^{-1}}$). In (a), the effect of varying the diameter D_i of the injector and of the distance H on the drop generation process, is shown. Here, $U = 0.85\ \mathrm{m\,s^{-1}}$, $Q_i = 30\,\mathrm{ml\,h^{-1}}$, $\mu_i = 5\,\mathrm{cP}$, $\mu_o = 1\,\mathrm{cP}$ ($\lambda_i = \mu_i/\mu_o = 5$) and $Re_o = \rho_o U L/\mu_o = 850$. Figure (b) shows the effects of varying both U and Q_i. Here, $\mu_i = 5\,\mathrm{cP}$, $\mu_o = 1\,\mathrm{cP}$ ($\lambda_i = 5$), $Re_o = 750$ (left) and $Re_o = 940$ (right). (c) For a fixed value of the flow rate ratio, $q_i = Q_i/\left(U\,L^2\right) = 0.011$, the images show the effect of varying the inner fluid viscosity for a value of the outer Reynolds number $Re_o = 940$. $D_i = 0.45$ mm in all images except at the botton of (a), where $D_i = 1.38$ mm. $H = 0.95$ mm in all images except: i) at the top left image of (a), where $H = 0.45$ mm and ii) at the bottom image of (a), where $H = 1.1$ mm.

stretched jet aligned with the axis of the extraction tube. Figure 5 shows that, in all cases considered, the drops formed by the capillary breakup of the inner liquid in the compound jet, are always encapsulated by the middle liquid surrounding it. The stretched jet is formed after injecting the two liquid flow rates Q_i and Q_m (see figure 2) within an

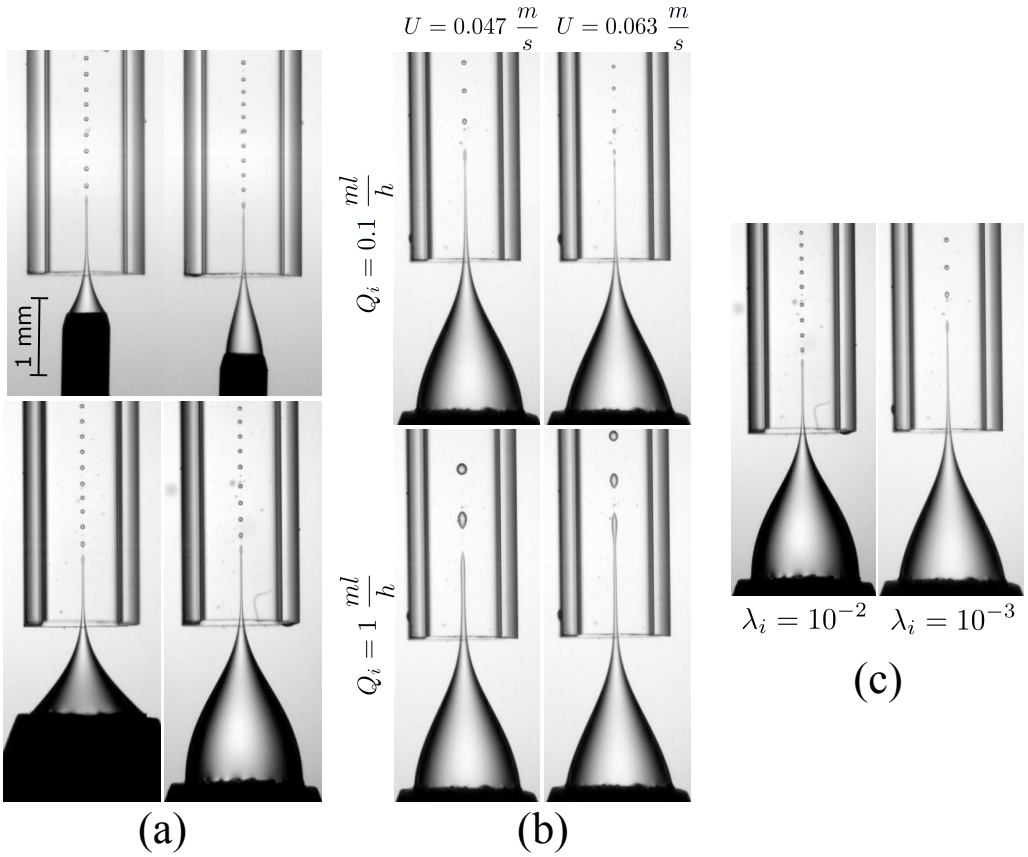

Figure 4: This figure shows the effect of varying the different parameters governing the generation of water in oil emulsions ($\sigma = 0.04\,\mathrm{N\,m^{-1}}$). In (a), the effect of varying the diameter D_i of the injector and the distance H on the drop generation process, is shown. Here, $U = 0.275\ \mathrm{m\,s^{-1}}$, $Q_i = 1\,\mathrm{ml\,h^{-1}}$, $\mu_i = 1\,\mathrm{cP}$, $\mu_o = 100\,\mathrm{cP}$, ($\lambda_i = 0.01$) and $Re_o = 2.65$. Figure (b) shows the effects of varying both U and Q_i. Here, $\mu_i = 1\,\mathrm{cP}$, $\mu_o = 1000\,\mathrm{cP}$, ($\lambda_i = 0.001$), $Re_o = 0.045$ (left) and $Re_o = 0.06$ (right). (c) For a fixed value of the flow rate ratio, $q_i = Q_i/(UL^2) = 0.001$, the images show the effect of varying the viscosity of the outer fluid. Here, $Re_o = 2.09$ (left) and $Re_o = 0.05$ (right). $D_i = 1.38$ mm in all images except at the top images of (a), where $D_i = 0.45$ mm. $H = 1.85$ mm in all images except: i) at the top left image of (a), where $H = 0.45$ mm and ii) at the top right image of (a) and at the bottom left image of (a), where $H = 0.95$ mm.

outer co-flow of mean velocity U verifying the conditions $Q_{i,m} \ll U\,L^2$, $Re_o \lesssim O(1)$ and

$$Ca'_o = \frac{\mu_o U}{(\sigma_i + \sigma_m)} > Ca^*(\lambda_i, \frac{Q_i}{U\,L^2})\,, \tag{2.3}$$

with $\lambda_i = \mu_i/\mu_o$. In equation (2.3), σ_i refers to the interfacial tension coefficient between the two liquids in the compound drop and σ_m to the corresponding value between the middle liquid and the continuous phase liquid. Similarly to the cases of generation of simple emulsions depicted in figures 3 and 4, the overall shape of the compound jet is dependent on the value of H for fixed values of $\mu_{i,m,o}$, Q_i, Q_m and U, but the diameter of the compound drops generated, is not (see figure 5a). The diameter of the drops can be

modulated, instead, by varying the different flow rates, Q_i, Q_m and $U\,L^2$, as it is shown in figure 5b. Figures 5c–d, where the influence of varying either μ_i or μ_m for fixed values of μ_o, U, Q_i and Q_m is illustrated, shows that the breakup of the compound jet gives rise to the generation of a train of uniformly-sized compound drops separated by a constant distance, a fact evidencing that the drop formation frequency is rather constant. Figure 5c also shows that tiny satellite drops of the middle fluid with diameters dependent on μ_m, are also generated.

3. Slender body theories describing the steady shapes of the liquid ligaments

The purpose of this section is to deduce the equations predicting, in the limits $Re_o \gg 1$ and $Re_o \ll 1$, the steady shapes of the simple or compound jets visualized in figures 3-5 from which drops are produced. The different set of equations describing the downstream evolution of the jet diameter will be based on a one-dimensional description for the flow within the jet and on an extension of the slender body theory developed in Castro-Hernández *et al.* (2012); Gordillo *et al.* (2014) describing the flow of the continuous phase. The main idea behind the slender body approximation is to represent the outer stream as the sum of an unperturbed flow field, calculated numerically using a commercial software (ANSYS Fluent), plus the perturbation introduced in the velocity and pressure fields by the presence of the jet. Let us point out here that the theoretical framework to be developed in what follows is applicable to describe axisymmetric flows in which either the inertial or the viscous terms can be neglected in the momentum equation.

As it is illustrated in figure 6, the perturbed flow field can be modeled as a continuous distribution of sources with intensities such that the kinematic condition is satisfied at the jet interface. Note that the unperturbed fields are calculated imposing the impermeability condition at the injection and extraction tubes without including the jet in the numerical simulations (see Evangelio *et al.* (2015) for details). As it is described in Castro-Hernández *et al.* (2012) and Gordillo *et al.* (2014), one of the advantages of decomposing the flow field as the addition of two fields, is the fact that the unperturbed solution depends only on the geometry of the emulsification device. Moreover, since the interface of the liquid jet is close to the axis of symmetry, the only influence of the unperturbed flow field in the one-dimensional equations describing the jet radius appears only through the functions $U_{xn}(X, R = 0)$ and $\partial^2 U_{xn}/\partial R^2(X, R = 0)$. Here, U_{xn} denotes the axial velocity of the outer liquid calculated numerically and the subscript n will be used in the following to denote the functions referred to the unperturbed fields. The analysis below will be carried out using variables which are made non-dimensional using U and L as the characteristic velocity and length scales. From now on, lower case variables will denote the dimensionless counterparts of the dimensional variables and, consequently,

$$x = \frac{X}{L}\,, \quad r = \frac{R}{L}\,, \quad u_{x,r} = \frac{U_{x,r}}{U}\,, \quad h = \frac{H}{L}\,, \tag{3.1}$$

with the origin of the x-coordinate located at the entrance of the extraction tube (see figure 1). The definition of the dimensionless pressure, depends on whether the outer flow is dominated by viscous or inertial stresses. More precisely, in the limits $Re_o \lesssim O(1)$ and $Re_o \gg 1$ the dimensionless pressure is respectively defined as

$$p = \frac{P\,L}{\mu_o\,U}\,, \quad p = \frac{P}{\rho_o\,U^2}\,. \tag{3.2}$$

In the following, the dimensionless outer velocity and pressure fields will be respectively

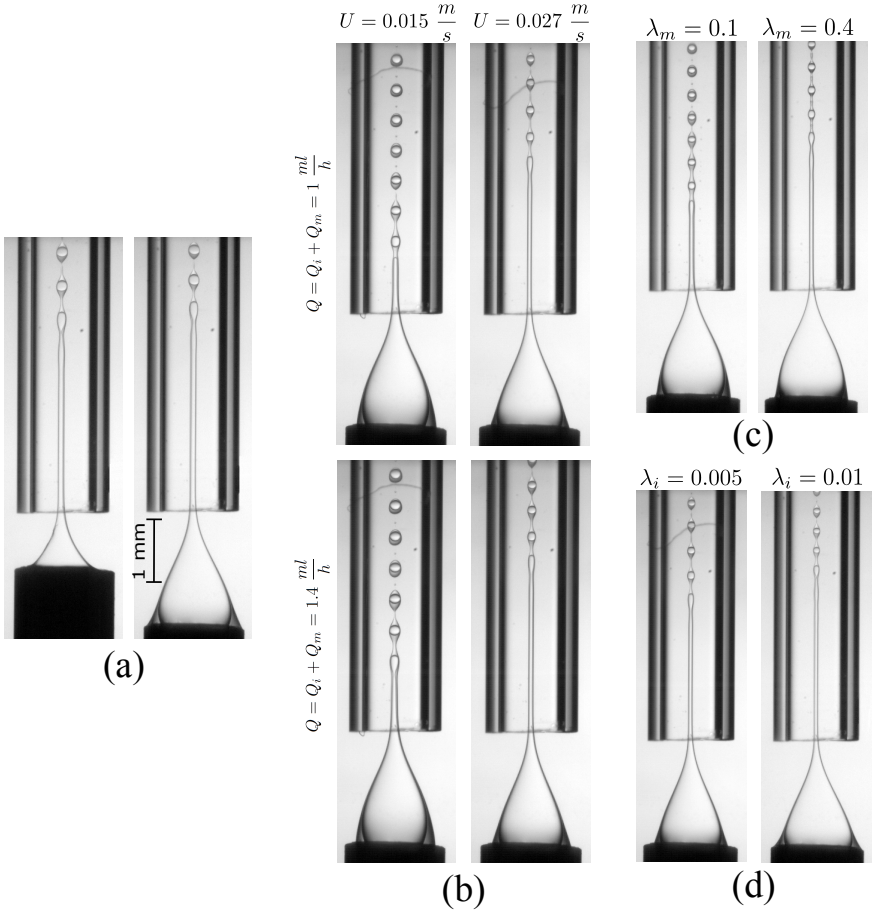

Figure 5: This figure shows the effect of varying the different parameters governing the generation of double emulsions. In (a), the effect of varying the distance of the injector to the extraction tube is depicted in the case of the middle fluid is Propylene Glycol and both the inner liquid and continuous phase are Silicone Oils. Therefore, $\sigma_{i,m} = 0.01\,\mathrm{N\,m^{-1}}$ with σ_i the interfacial tension coefficient between the inner and the middle fluid and σ_m the interfacial tension coefficient between the middle fluid and the continuous phase. Here, $\mu_i = 10\,\mathrm{cP}$, $\mu_m = 42\,\mathrm{cP}$, $\mu_o = 1000\,\mathrm{cP}$, $U = 0.02\,\mathrm{m\,s^{-1}}$, $Q_i = 0.5\,\mathrm{ml\,h^{-1}}$, $Q_m = 0.5\,\mathrm{ml\,h^{-1}}$ and, consequently, $q = (Q_i + Q_m)/(U\,L^2) = 0.014$ and $Re_o = 0.02$. Figure (b) shows the effects of varying both the outer fluid velocity and the total flow rate $Q = Q_i + Q_m$ on the generation of compound drops. In this case, the middle liquid is Propylene Glycol and both the inner and the continuous phase are different Silicone Oils: $\sigma_{i,m} = 0.01\,\mathrm{N\,m^{-1}}$, $\mu_i = 5\,\mathrm{cP}$, $\mu_m = 42\,\mathrm{cP}$, $\mu_o = 1000\,\mathrm{cP}$, $Re_o = 0.015$ (left) and $Re_o = 0.02$ (right). Figure (c) shows the effect of varying the middle liquid viscosity on the generation of compound drops. In this case, the middle liquid is the mixture of Glycerine+Water in two different proportions, while the inner liquid as well as the continuous phase are Silicone Oils of viscosities $\mu_i = 10\,\mathrm{cP}$ and $\mu_o = 1000\,\mathrm{cP}$ respectively. $\sigma_{i,m} = 0.03\,\mathrm{N\,m^{-1}}$. Left, $U = 0.045\ \mathrm{m\,s^{-1}}$, $Q_i = 1\,\mathrm{ml\,h^{-1}}$, $Q_m = 2\,\mathrm{ml\,h^{-1}}$, $\lambda_i = 0.01$, $\lambda_m = \mu_m/\mu_o = 0.1$, $Re_o = 0.043$. Right, $U = 0.045\ \mathrm{m\,s^{-1}}$, $Q_i = 2\,\mathrm{ml\,h^{-1}}$, $Q_m = 1\,\mathrm{ml\,h^{-1}}$, $\lambda_i = 0.01$, $\lambda_m = 0.4$, $Re_o = 0.043$. In these experiments, the ratio $q = (Q_i + Q_m)/(U\,L^2)$ is kept constant. Figure (d) shows the effect of varying the inner fluid viscosity on the generation of compound drops. In this case, the middle liquid is Propylene Glycol, $\mu_m = 42\,\mathrm{cP}$ and the inner and the continuous phase liquids are Silicone Oils. The outer fluid viscosity is kept constant to $\mu_o = 1000\,\mathrm{cP}$; therefore, $\lambda_m = 0.042$ and $\sigma_{i,m} = 0.01\,\mathrm{N\,m^{-1}}$. Left, $U = 0.014\ \mathrm{m\,s^{-1}}$, $Q_i = 0.3\,\mathrm{ml\,h^{-1}}$, $Q_m = 0.3\,\mathrm{ml\,h^{-1}}$, $\mu_i = 5\,\mathrm{cP}$, $\lambda_i = 5 \times 10^{-3}$, $Re_o = 0.013$. Right: $U = 0.025\ \mathrm{m\,s^{-1}}$,$Q_i = 0.5\,\mathrm{ml\,h^{-1}}$, $Q_m = 0.5\,\mathrm{ml\,h^{-1}}$, $\mu_i = 10\,\mathrm{cP}$, $\lambda_i = 10^{-2}$, $Re_o = 0.024$. In these experiments, the ratio $q = (Q_i + Q_m)/(U\,L^2)$ is kept constant. $H = 1.75$ mm in all cases except at the left image in (a), where $H = 0.9$ mm. In all cases, $D_i = 1$ mm and $D_m = 1.2$ mm.

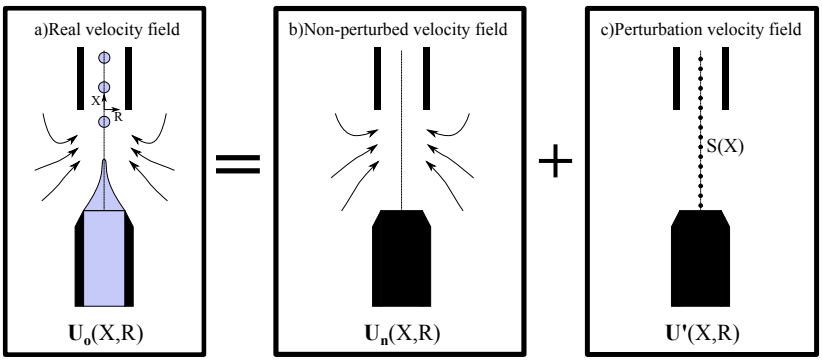

Figure 6: Sketch showing that the outer flow field (a) can be decomposed as the addition of two fields: the unperturbed flow field (b), which is calculated numerically using ANSYS Fluent and the perturbed flow field (c) associated with the presence of the jet. The perturbed velocity field can be quantified as a continuous line of sources of intensity $S(X)$ located at the axis of symmetry.

expressed as

$$\mathbf{u_o} = \mathbf{u_n} + \mathbf{u'} = [u_{xn}(x,r) + u'_x]\,\mathbf{e_x} + [u_{rn}(x,r) + u'_r]\,\mathbf{e_r}\,, \quad p_o = p_n + p'\,, \tag{3.3}$$

with $\mathbf{u'}$ and p' such that $|\mathbf{u'}| \ll \mathbf{u_n}$ and $p' \ll p_n$ indicating the perturbed velocity and pressure fields. Next, the analytical expression of the outer velocity field in the near axis region, which is where the jet is located, will be deduced. Note first that the Taylor series expansion of the unperturbed velocity field around $r = 0$ yields,

$$\mathbf{u_n} = u_{xn}(x,r)\mathbf{e_x} + u_{rn}(x,r)\mathbf{e_r} \simeq \left[u_{xn}(x,r=0) + \frac{1}{2}\frac{\partial^2 u_{xn}(x,r)}{\partial r^2}(x,r=0)r^2\right]\mathbf{e_x} + u_{rn}\mathbf{e_r} =$$
$$= \left[u_x(x) + f(x)r^2\right]\mathbf{e_x} + u_{rn}(x,r)\mathbf{e_r}\,, \tag{3.4}$$

with $u_x(x) = u_{xn}(x,r=0)$ and $f(x) = 1/2\,\partial^2 u_{xn}/\partial r^2(x,r=0)$. Now, making use of the continuity equation in cylindrical coordinates, $\partial u_{xn}/\partial x + (1/r)\partial(r\,u_{rn})/\partial r = 0$,

$$\frac{1}{r}\frac{\partial\,(r\,u_{rn})}{\partial r} = -\frac{\partial u_{xn}}{\partial x} = -\frac{d\,u_x}{d\,x} - r^2\frac{d^2\,f}{d\,x^2} \Rightarrow u_{rn} = -\frac{r}{2}\frac{d\,u_x}{d\,x} - \frac{r^3}{4}\frac{d\,f}{d\,x}\,. \tag{3.5}$$

Consequently, the equation for the near-axis outer velocity field (3.4) can be expressed as

$$\mathbf{u_n}(x,r) = \left[u_x(x) + f(x)r^2\right]\mathbf{e_x} + \left[-\frac{r}{2}\frac{du_x}{dx}(x) - \frac{r^3}{4}\frac{df}{dx}(x)\right]\mathbf{e_r}\,. \tag{3.6}$$

Since, in the limit $Re_o \gg 1$, the axial component of the outer velocity field for $r \ll 1$ can be approximated to a plug flow, setting $f = 0$ in equation (3.6), yields

$$\mathbf{u_n}(x,r) = u_x(x)\mathbf{e_x} + \left[-\frac{r}{2}\frac{d\,u_x}{d\,x}(x)\right]\mathbf{e_r}\,. \tag{3.7}$$

As it was pointed out in Castro-Hernández *et al.* (2012); Gordillo *et al.* (2014), the perturbed velocity field can be approximated to that generated by a continuous distribution

of sources of intensity $s(\overline{x})$, namely,

$$u'_x(x,r) = \frac{1}{2}\int_{-h}^{l_\infty} \frac{s(\overline{x})(x-\overline{x})}{\left[(x-\overline{x})^2+r^2\right]^{3/2}}\, d\overline{x}\,, \tag{3.8}$$

$$u'_r(x,r) = \frac{1}{2}\int_{-h}^{l_\infty} \frac{s(\overline{x})r}{\left[(x-\overline{x})^2+r^2\right]^{3/2}}\, d\overline{x}. \tag{3.9}$$

The integral in equation (3.9) was calculated in Castro-Hernández *et al.* (2012); Gordillo *et al.* (2014) as $u'_r(x,r) \simeq s(x)/r$, which is a fairly good approximation to the exact value of u'_r in equation (3.9) for all values of x, except in the region close to the injector, $x \simeq -h$. To improve the agreement between the predicted shapes of the jets and those observed experimentally, the integral (3.9) is approximated here as

$$u'_r(x,r) \simeq -\frac{s(x)}{2r}\left[\frac{x-l_\infty}{\sqrt{(x-l_\infty)^2+r^2}} - \frac{x+h}{\sqrt{(x+h)^2+r^2}}\right], \tag{3.10}$$

which is in excellent agreement with the exact value of the integral in equation (3.9) for all values of x.

We checked that equations (3.8)-(3.10) become independent of l_∞ for sufficiently high values of this parameter and, consequently, here we have set $l_\infty = 10$. Let us point out that, while the main contribution of the integral (3.9) was expressed analytically in (Castro-Hernández *et al.* (2012) and Gordillo *et al.* (2014)), in this contribution, the axial and the radial components of the perturbed velocity field will be calculated numerically or using the more accurate expression (3.10) respectively. Note now that, making use of the expression for $u'_r(x, r = r_j)$ given in equation (3.10), the intensity of the sources can be expressed as a function of the jet radius $r_j(x)$ by means of the kinematic condition at the jet interface,

$$\begin{aligned}
&\frac{dr_j(x)}{dx} = \frac{u_{rn}(x,r=r_j(x)) + u'_r(x,r=r_j(x))}{u_{xn}(x,r=r_j(x)) + u'_x(x,r=r_j(x))} \simeq \frac{u_{rn}(x,r=r_j(x)) + u'_r(x,r=r_j(x))}{u_{xn}(x,r=r_j(x))} \Rightarrow \\
&\Rightarrow u'_r(x,r=r_j(x)) = u_{xn}(x,r=r_j(x))\frac{dr_j(x)}{dx} - u_{rn}(x,r=r_j(x)) = \\
&= \left[u_x(x) + f(x)r_j^2\right]\frac{dr_j(x)}{dx} + \frac{r_j}{2}\frac{du_x(x)}{dx} + \frac{r_j^3}{4}\frac{df}{dx}(x)\,.
\end{aligned} \tag{3.11}$$

Making use of equations (3.10)-(3.11) it can be concluded that

$$s(x) = -2\frac{\left[u_x(x) + f(x)r_j^2\right] r_j \frac{dr_j(x)}{dx} + \frac{r_j^2}{2}\frac{du_x(x)}{dx} + \frac{r_j^4}{4}\frac{df}{dx}(x)}{\left[\frac{x-l_\infty}{\sqrt{(x-l_\infty)^2+r_j^2}} - \frac{x+h}{\sqrt{(x+h)^2+r_j^2}}\right]}\,. \tag{3.12}$$

Next, we will make use of the results expressed by (3.8)-(3.11) to deduce the equations describing the downstream evolution of the simple and compound jets in the cases $Re_o \ll 1$ and $Re_o \gg 1$.

3.1. *Equations for $r_j(x)$ and $r_i(x)$ in the limit $Re_o \ll 1$*

First of all let us point out that, since the perturbed velocity field given by equations (3.8)-(3.10) can be expressed as a function of a velocity potential, the pressure gradient

associated with $\mathbf{u}'$ is zero in the Stokes limit (Gordillo *et al.* 2014). Therefore, in the near axis region $r \ll 1$, the pressure gradient of the outer flow field can be expressed as

$$\frac{\partial p_o}{\partial x}(x,r) = \frac{\partial p_n}{\partial x} = \frac{d^2 u_x}{dx^2} + r^2 \frac{d^2 f}{dx^2} + 4f\,, \tag{3.13}$$

where use of the momentum equation in the limit $Re_o \to 0$ has been made (see Gordillo *et al.* (2014) for details). In the case of simple jets, the equation for r_j is deduced making use of the continuity equation (Gordillo *et al.* 2014),

$$q_i = \frac{Q_i}{UL^2} = \left[u_x(x) + f(x) r_j^2(x)\right] \pi r_j^2(x) - \frac{\pi r_j^4(x)}{8\lambda_i} \frac{dp_i(x)}{dx}\,. \tag{3.14}$$

In (3.14), the pressure gradient is calculated from the normal stress balance at the jet interface which, in the limit $\mu_o \gg \mu_i$, reads

$$\frac{dp_i}{d\,x}(x, r = r_j(x)) = \frac{d\,p_n}{d\,x}(x, r = r_j(x)) + \frac{d}{d\,x}\left[\frac{\chi}{Ca_o} - 2\left(\frac{\partial u_{rn}}{\partial r}(r = r_j) + \frac{\partial u_r'}{\partial r}(r = r_j)\right)\right]. \tag{3.15}$$

In equation (3.15), $\partial u_{rn}/\partial r(r = r_j) = -1/2 d\,u_x/d\,x - 3/4 r_j^2 d\,f/d\,x$,

$$\chi = \nabla \cdot \mathbf{n} = \frac{1}{r_j(1+\dot{r}_j^2)^{1/2}} - \frac{\ddot{r}_j}{(1+\dot{r}_j^2)^{3/2}}\,, \tag{3.16}$$

and dots denote derivatives with respect to x. From now on, we will use indistinctly either d/dx or a dot to indicate a derivative with respect to x. Therefore, the substitution of equation (3.13) into (3.15) yields

$$\frac{dp_i}{dx}(x, r = r_j(x)) = \frac{1}{Ca}\frac{d\chi}{dx} + 2\frac{d^2 u}{dx^2} + 4f + 3r_j \frac{dr_j}{dx}\frac{df}{dx} + + \frac{5}{2} r_j^2 \frac{d^2 f}{dx^2} - 2\frac{d}{dx}\left(\frac{\partial u_r'}{\partial r}(r = r_j)\right) \tag{3.17}$$

and once $d\,p_i/d\,x$ is expressed as a function of $r_j(x)$, u_x and f, the jet radius is calculated solving the equation

$$q_i = \left[u_x(x) + f(x) r_j^2(x)\right] \pi r_j^2(x) - \frac{\pi r_j^4(x)}{8\lambda_i}\left[\frac{1}{Ca}\frac{d\chi}{dx} + 2\frac{d^2 u}{dx^2} + 4f + 3r_j \frac{dr_j}{dx}\frac{df}{dx} + + \frac{5}{2} r_j^2 \frac{d^2 f}{dx^2} - 2\frac{d}{dx}\left(\frac{\partial u_r'}{\partial r}(r = r_j)\right)\right] \tag{3.18}$$

where

$$\frac{\partial\, u_r'}{\partial\, r}(x, r_j) = \frac{s(x)}{2}\left[\frac{\frac{(x-l_\infty)^3}{r_j^2} + 2(x - l_\infty)}{\left[(x-l_\infty)^2 + r_j^2\right]^{\frac{3}{2}}} - \frac{\frac{(x+h)^3}{r_j^2} + 2(x+h)}{\left[(x+h)^2 + r_j^2\right]^{\frac{3}{2}}}\right], \tag{3.19}$$

is deduced making use of equation (3.10).

Given the functions $u_x(x)$ and $f(x)$ characterizing a specific geometrical arrangement (see figure 7), the shape of the jet is calculated iteratively: a Newton-Raphson method is used to satisfy equation (3.18) at discrete collocation points, following a procedure which is quite similar to that described in Gordillo *et al.* (2014), being the main difference that equation (3.19) needs to be evaluated at the collocation points once the intensity of the sources $s(x)$ is calculated as a function of r_j by means of equation (3.12). The only boundary condition that needs to be imposed to the system of equations is $r_j(x = -h) = D_i/(2L)$ since the second condition is substituted by the discretized version of the

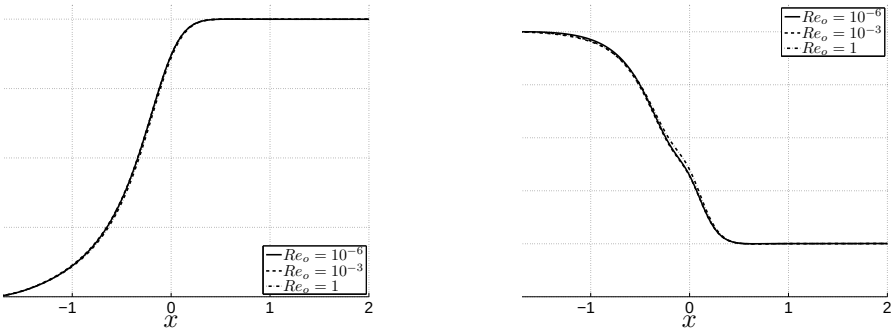

(a) (b)

Figure 7: Numerically calculated functions u_x and f in the Stokes limit for the particular case $H/L = 0.97$ and $D/L = 0.45$.

differential equation particularized at the very last node of the numerical domain (see Gordillo *et al.* (2014)).

In the analogous case of compound jets, the equations describing the positions of the inner and outer interfaces, $r_i(x)$ and $r_j(x)$ respectively (see the sketch in figure 2), are also deduced making use of the continuity equation for each of the two immiscible fluids in the jet, namely,

$$q_i = \frac{Q_i}{U\,L^2} = \left[u_x(x) + f(x) r_j^2(x)\right] \pi r_i^2(x) - \frac{\pi r_i^4(x)}{8\lambda_i} \frac{dp_i(x)}{dx}\,, \tag{3.20}$$

and

$$q_m = \frac{Q_m}{U\,L^2} = \left[u_x(x) + f(x) r_j^2(x)\right] \pi \left(r_j(x)^2 - r_i^2(x)\right)\,. \tag{3.21}$$

The validity of neglecting the contribution of the term proportional to the pressure gradient in equation (3.21), will be checked a posteriori, when the results of the model are compared with the experimental observations. Following the previous derivation, the only remaining step to deduce the differential equations for r_i and r_j is to express the pressure gradient $d\,p_i/dx$ as a function of r_j. This is done making use of the normal stress balance at the inner interface which, in the limit $\mu_m \gg \mu_i$ reads,

$$p_i(x, r = r_i(x)) = p_m(x, r = r_i(x)) + \frac{\chi_i}{Ca_i} + \lambda_m \left[\dot{u}_x(x) + 2 r_j(x) \dot{r}_j(x) f(x) + r_j^2(x) \dot{f}(x)\right]\,, \tag{3.22}$$

with $\lambda_m = \mu_m/\mu_o$ and

$$\chi_i = \frac{1}{r_i (1 + \dot{r}_i^2)^{1/2}} - \frac{\ddot{r}_i}{(1 + \dot{r}_i^2)^{3/2}}\,. \tag{3.23}$$

In equation (3.22), the expression for the term proportional to λ_m has been deduced consistently with a plug flow-type of velocity field for the middle liquid of the form,

$$\mathbf{u_m}(x, r) = \left[u_x(x) + f(x) r_j^2(x)\right] \mathbf{e_x} - \frac{r}{2} \left[\dot{u}_x(x) + 2 r_j(x) \dot{r}_j(x) f(x) + r_j^2(x) \dot{f}\right] \mathbf{e_r} \tag{3.24}$$

where use of the continuity equation has been made. In (3.22), the pressure p_m is deduced

from the normal stress balance at the outer interface which, in the limit $\mu_o \gg \mu_m$ reads,

$$p_m(x, r = r_j(x)) = p_o(x, r = r_j(x)) + \frac{\chi}{Ca_m} - 2\left[\frac{\partial u_{rn}}{\partial r}(r = r_j) + \frac{\partial u_r'}{\partial r}(r = r_j)\right], \quad (3.25)$$

with χ given in equation (3.16).

Therefore, taking the x-derivative of equations (3.22) and (3.25), with $\dot{p}_o$ given in equation (3.13) yields,

$$\begin{aligned}\dot{p}_i(x, r = r_i(x)) =& \frac{\dot{\chi}}{Ca_m} + 2\ddot{u}_x + 4f + 3r_j\dot{r}_j\dot{f} + \frac{5}{2}r_j^2\ddot{f} - 2\frac{d}{dx}\left(\frac{\partial u_r'}{\partial r}(r = r_j)\right) + \\ &+ \frac{\dot{\chi}_i}{Ca_i} + \lambda_m\left[\ddot{u}_x + 2\dot{r}_j^2 f + 2r_j\ddot{r}_j f + 4r_j\dot{r}_j\dot{f} + r_j^2\ddot{f}\right],\end{aligned} \quad (3.26)$$

with $Ca_m = \mu_o U/\sigma_m$ and $Ca_i = \mu_o U/\sigma_i$.

The substitution of equation (3.26) into (3.20) provides with the system of equations (3.20)-(3.21) for the two unknowns r_i and r_j, which needs to be complemented with the pair of equations (3.12) and (3.19) expressing $s(x)$ and $\partial u_r'/\partial r(r = r_j)$ as a function of r_j. The only boundary conditions that need to be imposed to the system of equations are $r_i(x = -h) = D_i/(2L)$ and $r_j(x = -h) = D_m/(2L)$. Both $r_i(x)$ and $r_j(x)$ are also calculated using a Newton-Raphson method: after a few iterations, the method converges and the pair of equations (3.20)-(3.21) are satisfied at discrete collocations points.

The excellent agreement between the observed and the calculated shapes exhibited in figures 8-9 confirms that the slender body theories developed in this section are a powerful tool to predict the shapes of simple and compound jets flowing within another immiscible liquid in realistic experimental situations. Let us point out that the reason why the model works so well in the vicinity of the injection tube, where the jet interface is not close to the axis of symmetry is thanks to the fact that the solution is dominated by the boundary condition at $x = -h$. Moreover, in this region, the dynamical effects of the outer stream are irrelevant, as well as the effect of the precise shape of the velocity profile at the exit of the injection tube.

3.2. *Equation for $r_j(x)$ in the limit $Re_o \gg 1$*

Contrarily to the low Reynolds number case considered above, the pressure gradient created by the perturbed velocity field is different from zero when $Re_o \gg 1$. Indeed, in the near axis region, where $u_{rn} \simeq -r/2\dot{u}_x$ since $f = 0$ in a plug type of flow, Bernoulli's equation reads, neglecting the higher order contribution $u_x'^2 \ll u_x u_x'$,

$$p_\infty = p_o(x) + \frac{1}{2}\mathbf{u_o}\cdot\mathbf{u_o} \simeq p_o + \frac{1}{2}\left[u_x^2 + 2u_x u_x' + \left(r^2/4\right)\dot{u}_x^2\right] \quad (3.27)$$

with u_x the unperturbed velocity in the limit $Re_o \gg 1$ at $r = 0$ calculated numerically (see figure 10) using ANSYS Fluent. Consequently, at the jet interface $r = r_j(x)$,

$$\dot{p}_o = -\left[u_x\dot{u}_x + \dot{u}_x u_x' + u_x\dot{u}_x' + \left(r_j^2/4\right)\dot{u}_x\ddot{u}_x\right], \quad (3.28)$$

with u_x' calculated using equation (3.8). The expression for the intensity of the sources deduced from the kinematic boundary condition yields, in the plug flow case $f = 0$,

$$s(x) = -2\frac{u_x(x)r_j\frac{dr_j(x)}{dx} + \frac{r_j^2}{2}\frac{du_x(x)}{dx}}{\left[\frac{x-l_\infty}{\sqrt{(x-l_\infty)^2+r_j^2}} - \frac{x+h}{\sqrt{(x+h)^2+r_j^2}}\right]}. \quad (3.29)$$

In the high Reynolds number limit, the continuity equation for the flow of liquid within the jet reads $q_i = Q_i/UL^2 = \pi u r_j^2$ and, therefore, the one dimensional momentum

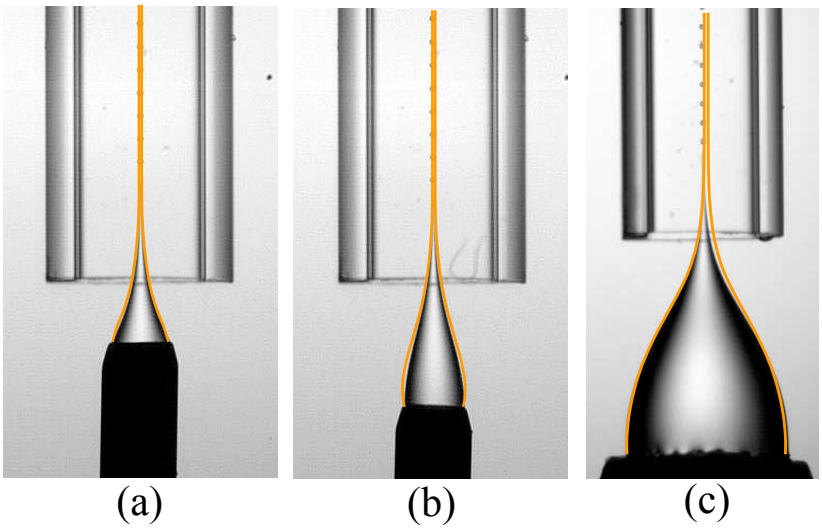

Figure 8: Simple jets: comparison between the predicted and the observed shapes in the case of $\lambda_i = 10^{-2}$ for different geometrical arrangements. In (a), $Ca_o = 1.04$, $Re_o = 3.92$, $Q_i = 0.5\,\mathrm{ml\,h^{-1}}$, $U = 0.206\,\mathrm{m\,s^{-1}}$. In (b), $Ca_o = 1.04$, $Re_o = 3.92$, $Q_i = 0.5\,\mathrm{ml\,h^{-1}}$, $U = 0.21\,\mathrm{m\,s^{-1}}$. In (c), $Ca_o = 1.04$, $Re_o = 3.92$, $Q_i = 0.5\,\mathrm{ml\,h^{-1}}$, $U = 0.21\,\mathrm{m\,s^{-1}}$. Notice that the agreement is excellent in spite of $Re_o \sim O(1)$. The agreement is equally good for the cases in which $Re_o \ll 1$.

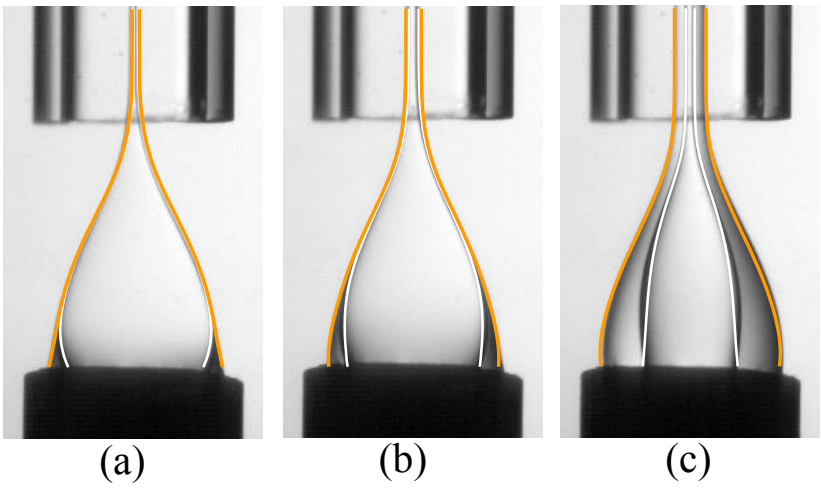

Figure 9: Compound jets: comparison between the predicted and the observed shapes for different values of the control parameters when the middle fluid is Propylene Glycol and the outer fluid viscosity is $\mu_o = 1000\,\mathrm{cP}$. In (a), $\lambda_m = 0.042$, $\lambda_i = 0.005$, $Ca'_o = \mu_o U/(\sigma_i + \sigma_m) = 0.7$, $Re_o = 0.027$, $Q_i = 0.1\,\mathrm{ml\,h^{-1}}$, $Q_m = 0.1\,\mathrm{ml\,h^{-1}}$, $U = 0.014\,\mathrm{m\,s^{-1}}$. In (b), $\lambda_m = 0.04$, $\lambda_i = 0.005$, $Ca'_o = 0.7$, $Re_o = 0.027$, $Q_i = 0.3\,\mathrm{ml\,h^{-1}}$, $Q_m = 0.3\,\mathrm{ml\,h^{-1}}$, $U = 0.014\,\mathrm{m\,s^{-1}}$. In (c), $\lambda_m = 0.04$, $\lambda_i = 0.01$, $Ca'_o = 1.79$, $Re_o = 0.067$, $Q_i = 1\,\mathrm{ml\,h^{-1}}$, $Q_m = 1\,\mathrm{ml\,h^{-1}}$, $U = 0.035\,\mathrm{m\,s^{-1}}$.

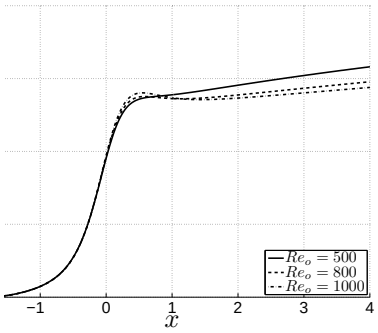

Figure 10: Numerically calculated function u_x in the high Reynolds number limit for the particular case $H/L = 0.97$ and $D/L = 0.45$.

equation deduced in Eggers & Dupont (1994) provides with the following equation for $r_j(x)$:

$$-\frac{2q_i^2\dot{r}_j}{\pi^2 r_j^5} = -\frac{\rho_o}{\rho_i}\left[\dot{p}_o + \frac{\sigma}{\rho_o U^2 L}\dot{\chi}\right] - \frac{6q_i}{\pi Re_o}\lambda_i \frac{\ddot{r}_j r_j - \dot{r}_j^2}{r_j^4}\frac{\rho_o}{\rho_i} \tag{3.30}$$

which is solved together with equations (3.8), (3.16), (3.28) and (3.29) using a Newton-Raphson method. The only boundary condition that needs to be imposed to the system of equations is $r_j(x = -h) = D_i/(2L)$.

Figure 11 also shows an excellent agreement between the calculated and the experimental shapes, a fact which gives support to the high Reynolds number slender body theory for capillary flows which, up to our knowledge, has been developed here for the first time. Let us point out that the the slight deviations observed in figure 11 are associated to the lateral oscillations of the jet triggered by Kelvin-Helmholtz instabilities.

4. Scaling the drop diameters and the drop formation frequencies

Assuming that the drop emission process is periodic, the frequency of drop formation f can be calculated as the ratio between the velocity at which the tip of the jet is convected downstream the region where drops are emitted, divided by a length ℓ_0, namely,

$$f = \frac{2\,U}{\ell_0} \quad \text{for} \quad Re_o \lesssim O(1) \quad \text{and} \quad f = \frac{U}{\ell_0} \quad \text{for} \quad Re_o \gg 1\,. \tag{4.1}$$

Notice that, in marked contrast with the process of bubble generation, in which the fragmentation of the gas ligament is forced by the pressure gradient of the outer flow (see Evangelio *et al.* (2015) for details), drops are created in this case as a consequence of the growth of a capillary instability. Consequently, ℓ_0 in equation (4.1) represents the length of the liquid cylinder for which capillary instabilities grow faster. The reason for the factor 2 multiplying U in equation (4.1), is due to the fact that the maximum velocity of a Poisueille velocity profile, which is reached where the jet is located i.e, at the axis of symmetry, is twice the mean velocity.

Denoting by Q the total flow rate of the liquids to be dispersed, i.e., $Q = Q_i$ in the case of generation of simple emulsions and $Q = Q_i + Q_m$ in the case of double emulsions, continuity demands that

$$\frac{\pi D_d^3}{6} f = Q\,, \tag{4.2}$$

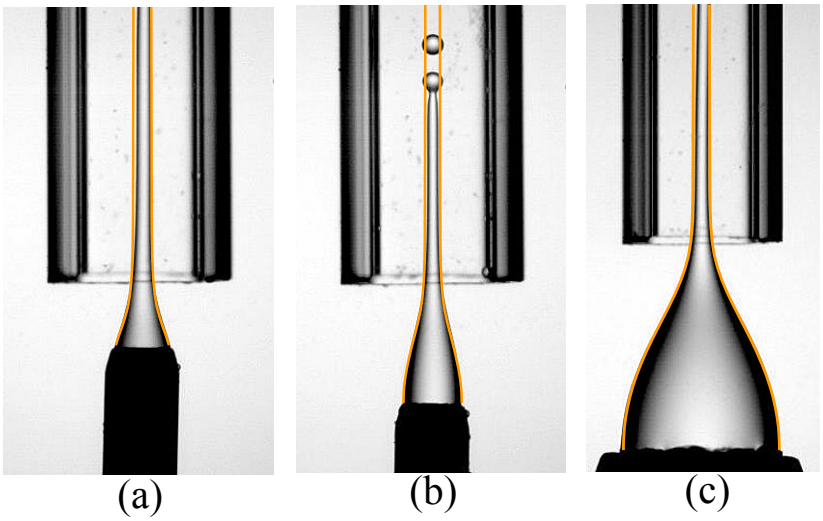

Figure 11: Comparison between the predicted and the observed shapes of steady liquid jets in the case of generation of oil drops in water, for which $Re_o \gg 1$ and $\sigma = 0.04\,\mathrm{N\,m^{-1}}$. In all the cases, $\lambda_i = 5$. In (a), $Q_i = 40\,\mathrm{ml\,h^{-1}}$, $U = 0.75\,\mathrm{m\,s^{-1}}$, $Re_o = 755$. In (b), $Q_i = 20\,\mathrm{ml\,h^{-1}}$, $U = 0.75\,\mathrm{m\,s^{-1}}$, $Re_o = 755$. In (c), $Q_i = 50\,\mathrm{ml\,h^{-1}}$, $U = 0.85\,\mathrm{m\,s^{-1}}$, $Re_o = 850$.

with D_d the outer diameter of the drop. Therefore, making use of equations (4.1)-(4.2),

$$\frac{D_d}{L} = \left[\frac{3\ell_0/L}{\pi}\,q\right]^{1/3} \quad \text{for} \quad Re_o \lesssim O(1) \quad \text{and} \quad \frac{D_d}{L} = \left[\frac{6\ell_0/L}{\pi}\,q\right]^{1/3} \quad \text{for} \quad Re_o \gg 1 \tag{4.3}$$

with $q = Q/(U\,L^2)$. Since, in the high Reynolds number case, continuity demands that $\ell_0/L \propto q^{1/2}$, equations (4.1)-(4.3) yield $f \propto U/(L\,q^{1/2})$ and $D_d/L \propto q^{1/2}$, being these scalings confirmed in figure 12 where, however, a significant dispersion in the experimental data is observed with respect to the expected trends. The dispersion depicted in figure 12 can be attributed to the lateral fluctuations experienced by the jets in the experiments of the type shown in figure 3, where $Re_o \sim 10^3$ is high enough for Kelvin-Helmholtz non axisymmetric instabilities to develop and, moreover, these values of the Reynolds number are also near the threshold for which the flow in the extraction tube experiences a laminar-turbulent transition.

In contrast, the production frequency of simple and compound drops is rather constant in the low Reynolds number case. This is due to the fact that the highly stretched liquid jets depicted in figures 4-5 are *steady* upstream the location where the drop production process takes place. Therefore, in the present case, it is worth calculating the wavelength of maximum amplification of capillary waves. For that purpose, we will make use of the dispersion relation,

$$\begin{aligned} D(\omega,k) = &-i\omega\left(2+\frac{k^2}{4\lambda_i}\right) + ik\left[2\,u_{x\infty} + f_\infty r_{j\infty}^2\left(4-\frac{2}{\lambda_i}\right)\right] - \frac{k^2}{8\lambda_i\,Ca} + \\ &+ i\,k^3\left(\frac{u_{x\infty}}{4\lambda_i} + \frac{f_\infty r_{j\infty}^2}{4\lambda_i}\right) + \frac{k^4}{8\lambda_i\,Ca} = 0\,, \end{aligned} \tag{4.4}$$

deduced in Gordillo *et al.* (2014) and in the Appendix for cylindrical jets and which,

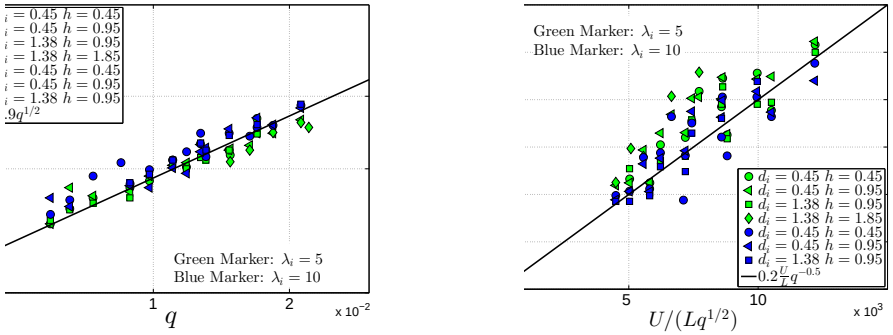

Figure 12: This figure shows that the diameters (a) and the frequencies (b) of the oil drops formed in water ($Re_o \gg 1$), follow the expected scalings $D_d \propto Lq^{1/2}$ and $f \propto U/(L\,q^{1/2})$ respectively. However, notice that the experimental data is rather dispersed with respect to the predicted trends.

in spite of its simplicity, is able to reproduce the results obtained using the much more involved dispersion relation due to Tomotika (1935). In (4.4) k is a real number and denotes the wavenumber -made dimensionless using the characteristic length $R_{j\infty}$-, ω is the complex frequency -made dimensionless using U and $R_{j\infty}$ as characteristic scales for the velocity and length respectively-, $u_{x\infty} = 2$, $f_\infty = -8$ are the asymptotic values of the functions in figure 7 and $r_{j\infty}$ is the solution of the continuity equation,

$$q_i = \left[u_{x\infty} + f_\infty r_{j\infty}^2\right] \pi r_{j\infty}^2 - \frac{\pi r_{j\infty}^4}{2\lambda_i} f_\infty \,, \tag{4.5}$$

which is deduced setting to zero all the x-derivatives in equation (3.14). Equation (4.5) will also be used in the case of generation of double emulsions: indeed, the meaning that the flow rate ratio q_i instead of q appears in equation (4.5), is due to the fact that the capillary breakup of the inner jet triggers the fragmentation of the compound jet. In equation (4.4), $Ca = Ca'_o = \mu_o U/(\sigma_i + \sigma_m)$ in the case of double emulsions i.e., from the point of view of the stability analysis, a compound jet can be viewed as a simple jet with an effective interfacial tension coefficient $\sigma = \sigma_i + \sigma_m$ whereas, in the case of simple jets, $Ca = Ca_o$.

The dispersion relation (4.4) is used to calculate the wavelength of maximum amplification of capillary disturbances as,

$$\frac{\ell_0}{L} = \frac{2\pi}{k_{max}} r_{j\infty} \tag{4.6}$$

with $k_{max}(Ca, \lambda_i) \in \Re$ indicating the wavenumber maximizing the imaginary part of the complex frequency ω in $D(\omega, k) = 0$.

Once ℓ_0/L is known from the solution of equations (4.4)-(4.6), both f and D_d are calculated making use of equations (4.1) and (4.3). The results obtained, depicted in figures 13-14, are in excellent agreement with the experimental measurements. Note also that the dispersion of the experimental data with respect to the expected trends is quite narrow, a fact confirming the periodicity of the drop emission process suggested in figures 4-5.

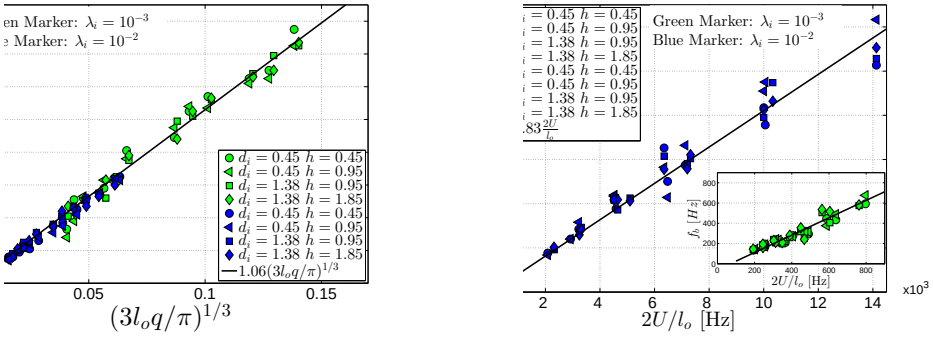

(a) (b)

Figure 13: Case of simple emulsions. This figure shows that the diameters (a) and the frequencies (b) of the simple emulsions generated when $Re_o \lesssim O(1)$, follow the expected scalings given in equations (4.3) and (4.1) respectively, with ℓ_o/L calculated by means of equation (4.6) and k_{max} deduced using (4.4). Notice that, in contrast with the high Reynolds number case, the dispersion of the experimental data with respect to the expected scaling is small.

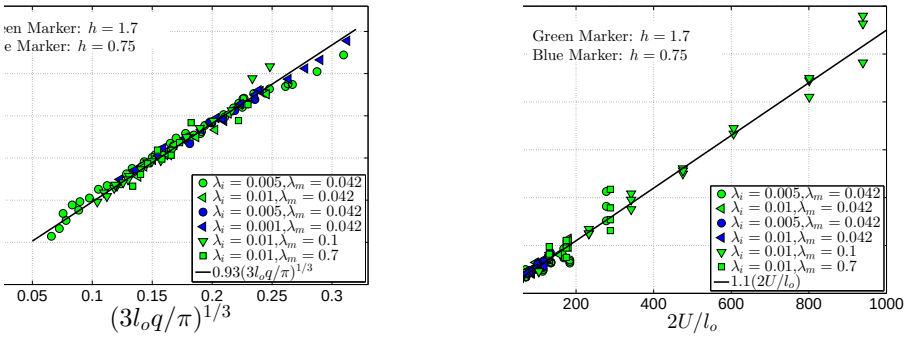

(a) (b)

Figure 14: Case of double emulsions. This figure shows that the diameters (a) and the frequencies (b) of the double emulsions generated when $Re_o \lesssim O(1)$, follow the expected scalings given in equations (4.3) and (4.1) respectively, with ℓ_o/L calculated by means of equation (4.6) and k_{max} deduced using (4.4). Notice that, in contrast with the high Reynolds number case, the dispersion of the experimental data with respect to the expected scaling is small. In this case, the capillary number is defined using an 'effective' interfacial tension coefficient, $\sigma = \sigma_i + \sigma_m$.

5. Stability Analysis in the limit of small Reynolds numbers

Now, it remains to answer the following question: which is the critical capillary number $Ca^*(\lambda_i, q_i)$ above which simple or compound drops are periodically produced as a consequence of the capillary breakup of highly stretched steady jets like those depicted in figures 4-5? It has been reported in Gañán Calvo & Riesco-Chueca (2006); Gañán Calvo *et al.* (2006, 2007); Gañán Calvo (2008) that the dependence of the critical capillary

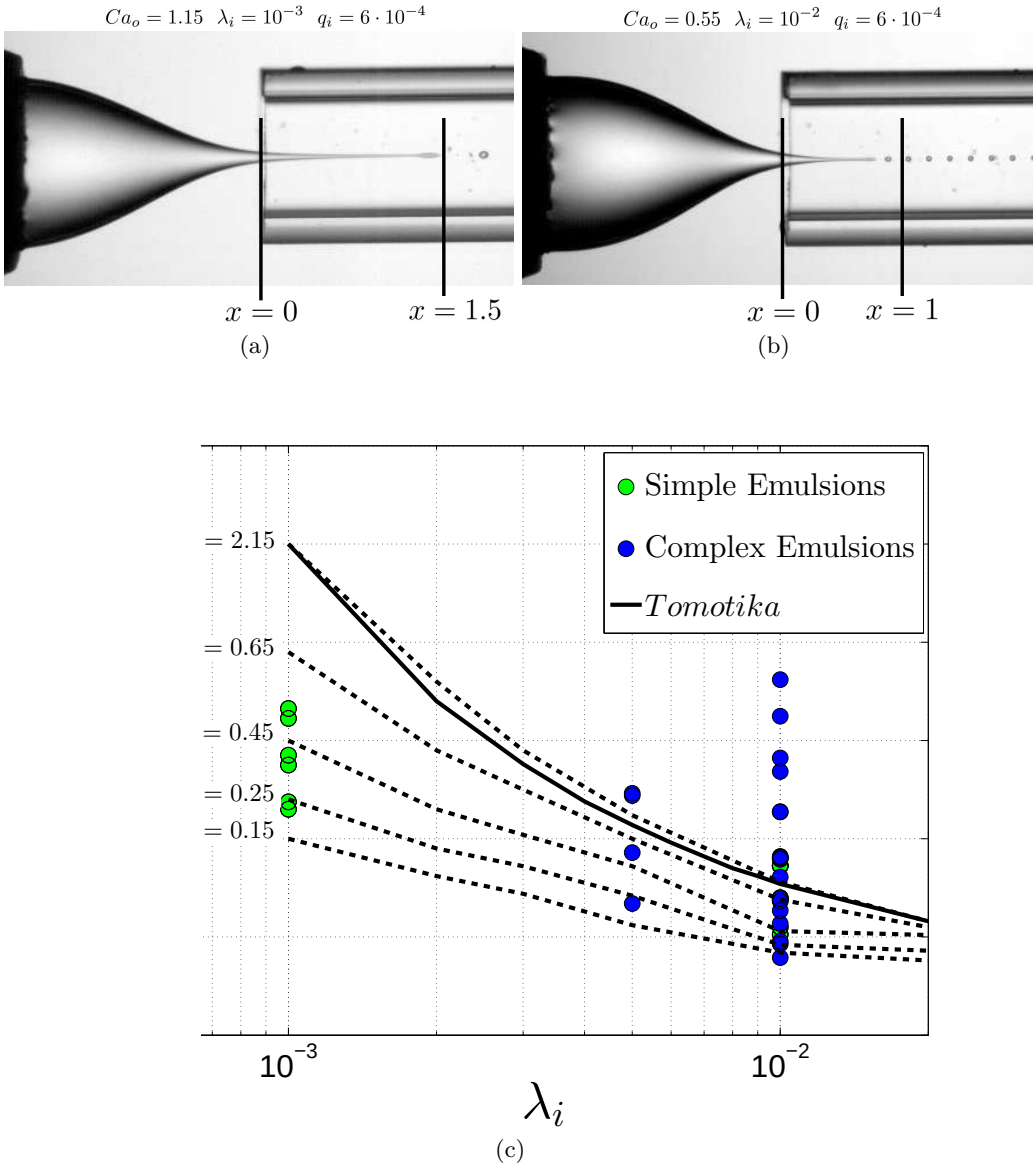

Figure 15: Figures (a)-(b) show the experimental shapes of simple jets for two values of the viscosity ratio. Figure (c) shows the experimental values of the capillary numbers for which simple or compound drops are generated as a consequence of the capillary breakup of highly stretched *steady* capillary jets. In the case of simple emulsions, $Ca_o = \mu_o U/\sigma$ and for double emulsions, $Ca_o' = \mu_o U/(\sigma_i + \sigma_m)$. Observe that, in our experiments, the minimum values of the capillary numbers above which steady jets and, therefore, droplets with a low size dispersion are produced, is well below the critical capillary number Ca^* calculated under the parallel flow assumption (dispersion relation (4.4), $Ca^* \simeq 0.139\lambda_i^{-1/2}$). However, if the x-dependent terms expressing that the unperturbed jet diameter decreases downstream are included in the analysis (dispersion relation 5.1), the agreement between observations and the predictions improves notably as x lies within the realistic values depicted in figures (a)-(b). Dashed lines represent the values of the critical capillary number calculated using the dispersion relation (5.1) for fixed values of x. All the results shown correspond to a value of the flow rate ratio $q_i = 10^{-3}$. The values of the critical capillary number, however, are insensitive to variations of q_i for $q_i \ll 1$.

number with the viscosity ratio is of the form $Ca^* = 0.139\lambda_i^{-1/2}$ in the type of flows generated in flow-focusing devices. This result is obtained by solving the pair of equations $D_T(\omega, k) = 0$ and $\partial D_T/\partial k = 0$ corresponding to $Im(\omega) = 0$, with $D_T(\omega, k)$ the dispersion relation given in equations (1)-(4) of Gañán Calvo, Herrada & Garstecki (2006), which is a generalization of the already rather involved dispersion relation given in equations (34)-(35) of Tomotika (1935). Motivated by this finding, we compare in figure 15 the values of the critical capillary numbers measured experimentally with the ones obtained solving the system $D(\omega, k) = 0$ and $\partial D/\partial k(\omega, k) = 0$ corresponding to $Im(\omega) = 0$, with $D(\omega, k) \neq D_T(\omega, k)$ the much simpler dispersion relation given in equation (4.4) -see the Appendix and Gordillo *et al.* (2014) for details-. Our calculations also provide with a value for the critical capillary number $Ca^* \simeq 0.139\lambda_i^{-1/2}$ (curve *Tomotika* in figure 15), independent of q_i for $q_i \ll 1$ in a much more straightforward way than that followed in Gañán Calvo & Riesco-Chueca (2006); Gañán Calvo *et al.* (2006, 2007); Gañán Calvo (2008); Herrada *et al.* (2010), but do *not* reproduce the experimental observations. The reason behind this discrepancy is associated with the fact that the dispersion relation (4.4) has been deduced assuming that the jet is cylindrical, in marked contrast with the experimental evidence depicted in figures 4-5 and 15a-b, where it is shown that drops are produced from the breakup of capillary jets experiencing a strong stretching in the downstream direction. In Gordillo *et al.* (2014), we described a new stabilization mechanism which is only present in converging capillary jets, i.e., in jets such that $\dot{r}_j(x) < 0$ and also found that the values of the critical capillary number for the flow to be globally stable, namely, for steady jets to be produced, are smaller than in the case of cylindrical jets. Moreover, in order to circumvent solving the equations for the global stability analysis, we also suggested in Gordillo *et al.* (2014) that the higher stability exhibited by stretched capillary jets could be qualitatively explained and quantified, in a first approximation and thanks to the fact that the unperturbed flow is slender i.e., $dr_{j0}/dx(x) \ll 1$ with $r_{j0}(x)$ the unperturbed jet radius, by performing a *local* spatio-temporal stability analysis using the dispersion relation (see the Appendix for details)

$$
\begin{aligned}
D'(\omega, k, x) = &-i\omega\left(2 + \frac{k^2}{4\lambda_i} - ik\frac{\dot{r}_{j0}}{2\lambda_i}\right) + ik\left[2\,u_x + fr_{j0}^2\left(4 - \frac{2}{\lambda_i}\right) + \frac{\dot{r}_{j0}}{2\,Ca\,\lambda_i}\right] \\
&- k^2\left[\frac{1}{8\lambda_i\,Ca} - \frac{r_{j0}\dot{u}_x}{2\lambda_i} - \frac{r_{j0}^3\dot{f}}{\lambda_i} - \dot{r}_{j0}\left(\frac{7}{4\lambda_i}r_{j0}^2 f + \frac{u_x}{4\lambda_i}\right)\right] + \\
&+ i\,k^3\left(\frac{u_x}{4\lambda_i} + \frac{fr_{j0}^2}{4\lambda_i} - \frac{5\dot{r}_{j0}}{8\,Ca\lambda_i}\right) + \frac{k^4}{8\lambda_i\,Ca} + \beta(x) = 0\,,
\end{aligned}
\tag{5.1}
$$

with

$$
\beta(x) = 2\frac{d}{dx}\left(u_x\, r_{j0}\right) + \frac{\dot{r}_{j0}^2 + \ddot{r}_{j0}r_{j0}}{4\lambda_i Ca} + 4r_{j0}^3\dot{f} - \frac{2r_{j0}^3\dot{f}}{\lambda_i} + fr_{j0}^2\dot{r}_{j0}\left(12 - \frac{6}{\lambda_i}\right). \tag{5.2}
$$

In (5.1)-(5.2), $r_{j0}(x)$, $u_x(x)$, $f(x)$, $\omega(x) = \Omega R_{j0}(x)/U$ and $k(x) = KR_{j0}(x)$, are slowly varying functions of x, with Ω and K the dimensional frequency and wavenumber respectively. Notice that $D'(\omega, k, x \gtrsim O(1)) \to D(\omega, k)$ since $\dot{u}_x(x \gtrsim O(1)) \to 0$, $\dot{r}_{j0}(x \gtrsim O(1)) \to 0$ and $\dot{f}(x \gtrsim O(1)) \to 0$.

In figure 15 we have calculated $Ca^*(\lambda_i, q_i)$ for fixed values of x by finding the values of the critical capillary number in the dispersion relation (5.1) for given values of λ_i and q_i i.e., by solving the system $D'(\omega, k, x) = 0$ and $\partial D'/\partial k(\omega, k, x) = 0$ corresponding to $Im(\omega) = 0$. The result, depicted in figure 15, shows that the effect of decreasing the value of x in equations (5.1)-(5.2) (which is equivalent to increase the value of $|\dot{r}_{j0}|$ and therefore

decrease the slenderness of the flow) is to decrease the value of the critical capillary number with respect to that predicted by the dispersion relation (4.4) corresponding to the case of purely cylindrical jets. Interestingly enough, the results obtained using the range of values of x for which drops are emitted from the tip of the jets (see figure 15a-b), are in good agreement with the experimental observations. Let us emphasize here that, as it was shown in Gordillo *et al.* (2014), the higher stability exhibited by the types of stretched jets described here *is not associated* with the term representing the stretching of the fluid elements, $2r_{j0}\dot{u}_x$, which is well known to promote the stabilization of the flow (Eggers & Villermaux 2008).

Thanks to the strong stretching experienced by the simple or compound capillary jets generated using the *confined selective withdrawal* geometry presented in Evangelio *et al.* (2015), the critical capillary number above which drops are regularly produced as a consequence of the capillary breakup of a steady jet, is below the corresponding values characterizing other methodologies, like flow focusing (Gañán Calvo & Riesco-Chueca 2006; Gañán Calvo *et al.* 2006, 2007; Gañán Calvo 2008; Herrada *et al.* 2010). Therefore, thanks to the fact that the jets produced here are less slender than the jets created using other technologies, the confined selective withdrawal method possesses the advantage of producing simple or compound drops in a controllable way for comparatively small values of the outer capillary number, with the subsequent saving of energy and of outer liquid.

6. Conclusions

In this contribution, we have presented a practical method for the generation of simple or double emulsions, based on the capillary breakup of highly stretched capillary jets. These jets are produced when either a liquid or a couple of them are injected from either a nozzle or a coaxial nozzle within a coflow of another liquid flowing from a pressurized reservoir towards a long extraction tube. The emulsions generated in such a way are composed of uniformly-sized micro droplets if the Reynolds number characterizing the flow of the continuous phase, Re_o, is of order unity or smaller and the capillary number is above a critical value Ca^* of order unity. Under these conditions, our theoretical analysis provides with analytical expressions for the drop generation frequencies, f, and for the diameters of the drops produced, D_d. The equations for f and D_d are expressed as a function of the width of the extraction tube L, the mean velocity of the outer liquid in the extraction tube U, and of the following dimensionless parameters: the viscosity ratio $\lambda_i = \mu_i/\mu_o$, with μ_i and μ_o the viscosities of the inner and outer fluids respectively, the capillary number $Ca = \mu_o U/\sigma$, with σ the interfacial tension coefficient, and the flow rate ratio $q_i = Q_i/(U\,L^2)$, with Q_i the flow rate of the inner fluid. In the case of double emulsions, the parameter $\sigma = \sigma_i + \sigma_m$ in the definition of Ca, represents the addition of σ_i, which is the interfacial tension coefficient between the inner and the middle fluids and σ_m, which is the corresponding coefficient between the middle fluid and the continuous phase. The outer diameters of the drops composing the double emulsions are also dependent on the parameter $q = Q/(U\,L^2)$, with Q the sum of the flow rates of the inner and middle fluids. The equations provided for f and D_d are valid whenever $Ca > Ca^*(\lambda_i, q_i)$, with $Ca^* \simeq Ca^*(\lambda_i)$ in the limit $q_i \ll 1$. This fact indicates that uniformly sized droplets with arbitrary small diameters can be produced using this methodology. This is so because, under these circumstances, the analysis predicts that the simple or compound capillary jets are globally stable namely, steady, at the entrance of the extraction tube and, in addition, our results indicate that the drop formation frequencies are those for which the capillary instabilities in the cylindrical portion of the jet, grow faster. The values of Ca^* above which a steady jet is formed, namely, the flow is globally stable, are well

predicted by a *local* spatio-temporal stability analysis, but only when the leading order terms expressing that the unperturbed solution varies downstream, are included in the analysis. In agreement with the experimental observations, our theory reveals that the highly stretched capillary jets generated using the present design are more stable than the slightly convergent cylindrical jets generated using other methodologies. This is the reason behind the fact that the critical capillary numbers above which stable jets are produced in the confined selective withdrawal geometry, are smaller than in the flow focusing one, a geometry for which it has been reported that the dependence of the critical capillary number with the viscosity ratio is of the form $Ca^* = 0.139\lambda_i^{-1/2}$ (Gañán Calvo & Riesco-Chueca 2006; Gañán Calvo *et al.* 2006, 2007; Gañán Calvo 2008).

Moreover, since the analytical description of capillary jets surrounded by another liquid is still far from being comparable to the advances accomplished in the analysis of the analogous case of liquid jets in air, we have also provided a theoretical framework, based on a slender body approach, to describe the *steady* shapes of axisymmetric simple or compound jets flowing within an immiscible liquid in the limits $Re_o \gg 1$ and $Re_o \lesssim O(1)$. Our theory is in excellent agreement with experimental observations.

This work has been supported by the Spanish MINECO under Project DPI2014-59292-C3-2-P, partly financed through European funds. The authors are grateful to Prof. Ignacio González Loscertales for providing us with a coaxial injection tube.

Appendix A. Local stability analysis of steady jets at low values of the Reynolds number

The dispersion relation to be deduced in what follows is built up starting from the unsteady continuity equation

$$\frac{\partial r_j^2}{\partial t} + \frac{\partial}{\partial x}\left[\left(u_x + f r_j^2\right) r_j^2 - \frac{r_j^4}{8\lambda_i}\frac{\partial p_i}{\partial x}\right] = 0\,, \tag{A 1}$$

which needs to be solved together with the kinematic condition at the jet interface, which differs from equation (3.11) in that, in this case, unsteady terms need to be retained:

$$u_r' = \frac{\partial r_j}{\partial t} + \left[u_x(x) + f(x) r_j^2\right]\frac{dr_j(x)}{dx} + \frac{r_j}{2}\frac{du_x(x)}{dx} + \frac{r_j^3}{4}\frac{df}{dx}(x)\,. \tag{A 2}$$

In equations (A 1)-(A 2), the dimensionless time is related to its dimensional counterpart as $t = TU/L$.

Since the *local* stability analysis will be performed in a portion of the jet which is far from the nozzle, where the flow is slender, i.e., where $dr_{j0}/dx \ll 1$, the perturbed radial velocity field created by the presence of the jet is approximated here, following the explanation given after equation (3.9), as

$$u_r' \simeq \frac{s(x,t)}{r} \Rightarrow \frac{\partial u_r'}{\partial r}(r = r_j) = -\frac{u_r'}{r_j}\,. \tag{A 3}$$

Introducing equations (A 2)-(A 3) into (3.17) and substituting the resulting expression into the unsteady mass conservation equation (A 1), yields the following dimensionless

partial differential equation for $r_j(x,t)$,

$$\frac{\partial r_j}{\partial t}\left[2r_j+\frac{1}{4\lambda_i}\left(2r_j\left(\frac{\partial r_j}{\partial x}\right)^2+r_j^2\frac{\partial^2 r_j}{\partial x^2}\right)\right]-\frac{1}{2\lambda_i}r_j^2\frac{\partial r_j}{\partial x}\frac{\partial}{\partial x}\left(\frac{\partial r_j}{\partial t}\right)-\frac{1}{4\lambda_i}r_j^3\frac{\partial^2}{\partial x^2}\left(\frac{\partial r_j}{\partial t}\right)+$$
$$+\frac{\partial}{\partial x}\left[\left(u_x+fr_j^2\right)r_j^2+\frac{1}{8\lambda_i}\left(-3r_j^4\frac{\mathrm{d}^2u_x}{\mathrm{d}x^2}-3\,r_j^6\frac{\mathrm{d}^2f}{\mathrm{d}x^2}-4fr_j^4-Ca^{-1}\,r_j^4\frac{\partial\chi}{\partial x}-6r_j^5\frac{\partial r_j}{\partial x}\frac{\mathrm{d}f}{\mathrm{d}x}-\right.\right.$$
$$\left.\left.-2\left(\frac{\partial r_j}{\partial x}\right)^2 fr_j^4+2r_j^2\left(\frac{\partial r_j}{\partial x}\right)^2 u_x-2r_j^3\frac{\partial r_j}{\partial x}\frac{\mathrm{d}u_x}{\mathrm{d}x}-2u_xr_j^3\frac{\partial^2 r_j}{\partial x^2}-2fr_j^5\frac{\partial^2 r_j}{\partial x^2}\right)\right]=0\,. \tag{A 4}$$

Assuming that the wavelength of the perturbation is much smaller than the length along which the steady jet radius experiences variations of its same order of magnitude, with this condition clearly verified for $x\gtrsim O(1)$, we look for traveling-wave solutions to equation (A 4), of the form

$$r_j=r_{j0}(x)+e^{i\left(\bar{k}x-\bar{\omega}\,t\right)}r_{j1} \tag{A 5}$$

with r_{j0} the unperturbed jet radius. In equation (A 5), $\bar{k}=KL$ and $\bar{\omega}=\Omega L/U$ indicate, respectively, the dimensionless counterparts of the dimensional wavenumber, K, and of the dimensional frequency, Ω. Once the ansatz (A 5) is introduced into equation (A 4), and retaining only linear terms in r_{j1} in the resulting expression yields,

$$D'(\omega,k,x)=-i\omega\left(2+\frac{k^2}{4\lambda_i}-ik\frac{\dot{r}_{j0}}{2\lambda_i}\right)+ik\left[2\,u_x+fr_{j0}^2\left(4-\frac{2}{\lambda_i}\right)+\frac{\dot{r}_{j0}}{2\,Ca\,\lambda_i}\right]$$
$$-k^2\left[\frac{1}{8\lambda_i\,Ca}-\frac{r_{j0}\dot{u}_x}{2\lambda_i}-\frac{r_{j0}^3\dot{f}}{\lambda_i}-\dot{r}_{j0}\left(\frac{7}{4\lambda_i}r_{j0}^2f+\frac{u_x}{4\lambda_i}\right)\right]+ \tag{A 6}$$
$$+\,i\,k^3\left(\frac{u_x}{4\lambda_i}+\frac{fr_{j0}^2}{4\lambda_i}-\frac{5\dot{r}_{j0}}{8\,Ca\lambda_i}\right)+\frac{k^4}{8\lambda_i\,Ca}+\beta(x)=0\,,$$

with

$$\beta(x)=2\frac{d}{dx}\left(u_x\,r_{j0}\right)+\frac{\dot{r}_{j0}^2+\ddot{r}_{j0}r_{j0}}{4\lambda_i Ca}+4r_{j0}^3\dot{f}-\frac{2r_{j0}^3\dot{f}}{\lambda_i}+fr_{j0}^2\dot{r}_{j0}\left(12-\frac{6}{\lambda_i}\right)\,. \tag{A 7}$$

In (A 6) the *local* dimensionless variables $\omega(x)=\bar{\omega}r_{j0}(x)\sim O(1)$ and $k=\bar{k}\,r_{j0}(x)\sim O(1)$, have been defined. To deduce the dispersion relation (A 6) we have retained only order unity terms as well as the leading order non parallel terms, i.e., those with an order of magnitude $\sim O(\dot{r}_{j0}(x))\ll 1$. The interest reader is directed to the Appendix of Gordillo *et al.* (2014) for further algebraic details.

REFERENCES

Ambravaneswaran, B., Subramani, H., Philips, S. & Basaran, O. 2004 Dripping-jetting transitions in a dripping faucet. *Phys. Rev. Lett.* **93**, 034501.

Anna, S.L. 2016 Droplets and bubbles in microfluidic devices. *Ann. Rev. Fluid Mech.* **48**, 285–309.

Anna, S.L., Bontoux, N. & Stone, H.A. 2003 Formation of dispersions using flow focusing in microchannels. *Appl. Phys. Lett.* **82**, 364–366.

Barrero, A. & Loscertales, I. G. 2007 Micro- and nanoparticles via capillary flows. *Ann. Rev. Fluid Mech.* **39**, 89–106.

Basaran, O., Gao, H. & Bhat, P. 2013 Nonstandard inkjets. *Ann. Rev. Fluid Mech.* **45**, 85–113.

Gañán Calvo, A.M. 1998 Generation of steady liquid microthreads and micron-sized monodisperse sprays in gas streams. *Phys. Rev. Lett.* **80**, 285–288.

Gañán Calvo, A.M. 2008 Unconditional jetting. *Phys. Rev. E* **78**, 026304.

Gañán Calvo, A.M., Herrada, M. & Garstecki, P. 2006 Bubbling in unbounded coflowing liquids. *Phys. Rev. Lett.* **96**, 124504.

Gañán Calvo, A.M. & Riesco-Chueca, P. 2006 Jetting-dripping transition of a liquid jet in a lower viscosity co-flowing immiscible liquid: the minimum flow rate in flow focusing. *J. Fluid Mech.* **553**, 75–84.

Gañán Calvo, A.M. González, R., Riesco-Chueca, P. & Herrada, M. 2007 Focusing capillary jets close to the continuum limit. *Nature Physics* **3**, 737–742.

Castro-Hernández, E., Campo-Cortés, F. & Gordillo, J. M. 2012 Slender-body theory for the generation of micrometre-sized emulsions through tip streaming. *J. Fluid Mech.* **698**, 423–445.

Chauhan, A., Maldarelli, C., Papageorgiou, D.T. & Rumschitzki, D.S. 2000 Temporal instability of compound threads and jets. *J. Fluid Mech.* **420**, 1–25.

Chong, D., Liu, X., Ma, H., Huang, G., Han, Y., Cui, X., Yan, J. & Xu, F. 2015 Advances in fabricating double-emulsion droplets and their biomedical applications. *Microfluids and Nanofluids* **19**, 1071–1090.

Cohen, I., Li, H., Hougland, J., Mrksich, M. & Nagel, S. 2001 Using selective withdrawal to coat microparticles. *Science.* **292**, 265–7.

Collins, R. T., Sambath, K., Harris, MT. & Basaran, O. 2013 Universal scaling laws for the disintegration of electrified drops. *PNAS.* **110**, 4905–4910.

Driessen, T., Sleutel, P., Dijksman, F., Jeurissen, R. & Lohse, D. 2014 Control of jet breakup by a superposition of two rayleigh-plateau-unstable modes. *J. Fluid Mech.* **749**, 275–296.

Eggers, J. & Dupont, T.F 1994 Drop formation in a one-dimensional approximation of the navier-stokes equation. *J. Fluid Mech.* **262**, 205–221.

Eggers, J. & Villermaux, E. 2008 Physics of liquid jets. *Rep. Prog. Phys.* **71** (3), 036601/1–79.

Evangelio, A., Campo-Cortés, F. & Gordillo, J. M. 2015 Pressure gradient induced generation of microbubbles. *J. Fluid Mech.* **778**, 653–668.

Fernández-Nieves, A., Vitelli, V., Utada, A.S., Link, D.R., Márquez, M., Nelson, D. R. & Weitz, D. 2007 Novel defect structures in nematic liquid crystal shells. *Phys. Rev. Lett.* **99**, 157801.

García, F.J. & Castellanos, A. 1994 One-dimensional models for slender axisymmetric viscous liquid jets. *Phys. Fluids* **6(8)**, 2676–2689.

Garstecki, P., Fuerstman, M., Stone, H. & Whitesides, G. 2006 Formation of droplets and bubbles in a microfluidic t-junction-scaling and mechanism of break-up. *Lab On a Chip* **6**, 437–446.

Garti, Nissim. 1997 Double emulsions: scope, limitations and new achievements. *Colloids and Surfaces.* **123-124**, 233–246.

Gordillo, J. M., Sevilla, A. & Campo-Cortés, F. 2014 Global stability of stretched jets: conditions for the generation of monodisperse micro-emulsions using coflows. *J. Fluid Mech.* **738**, 335–357.

Guerrero, J., González, H. & García, F.J. 2012 Spatial modes of capillary jets, with application to surface stimulation. *J. Fluid Mech.* **702**, 354–377.

Herrada, M.A., Montanero, J.M., Ferrera, C. & Gañán Calvo, A.M. 2010 Analysis of the dripping-jetting transition in compound capillary jets. *J. Fluid Mech.* **649**, 523–536.

Hertz, B. & Hermanrud, B. 1983 A liquid compound jet. *J. Fluid Mech.* **131**, 271–287.

Lopez-Leon, T., Koning, V., Devaiah, K. B. S., Vitelli, V. & Fernández-Nieves, A. 2011 Frustrated nematic order in spherical geometries. *Nature Physics* **7**, 391–394.

Loscertales, I. G., Barrero, A., Guerrero, I., Cortijo, R., Márquez, M. & Gañán Calvo, A.M. 2002 Micro/nano encapsulation via electrified coaxial liquid jets. *Science.* **295**, 1695–1698.

Loscertales, I. G., Barrero, A., Márquez, M., Spretz, R., Velarde-Ortiz, R. & Larsen, G. 2004 Electrically forced coaxial nanojets for one-step hollow nanofiber design. *J. Am. Chem. Soc.* **126**, 5376–5377.

Marín, A.G., Loscertales, I. G., Márquez, M. & Barrero, A. 2007 Simple and double emulsions via coaxial jet electrosprays. *Phys. Rev. Lett.* **98**, 014502.

de la Mora, JF. 2007 The fluid dynamics of taylor cones. *Ann. Rev. Fluid Mech.* **39**, 217–423.

Nabavi, S., Vladisavljević, G., Gu, S. & Ekanem, E. 2015 Double emulsion production in glass capillary microfluidic device: Parametric investigation of droplet generation behaviour. *Chem. Eng. Science* **130**, 183–196.

Oh, H., Kim, S., Baek, J., Seong, G. & Lee, S. 2006 Hydrodynamic micro-encapsulation of aqueous fluids and cells via 'on the fly' photopolymerization. *J. Micromech. Microeng* **16**, 285–291.

Rodríguez-Rodríguez, J., Gordillo, J. M. & Martínez-Bazán, C. 2006 Breakup time and morphology of drops and bubbles in a high Reynolds number flow. *J. Fluid Mech.* **548**, 69–86.

Rubio-Rubio, M., Sevilla, A. & Gordillo, J. M. 2013 On the thinnest steady threads obtained by gravitational stretching of capillary jets. *J. Fluid Mech.* **729**, 471–483.

Sanz, A. & Meseguer, J. 1985 One-dimensional linear analysis of the compound jet. *J. Fluid Mech.* **159**, 55–68.

Shah, R., Shum, H., Rowat, A., Lee, D., Agresti, J., Utada, A., Chu, L., Kim, J., Fernández-Nieves, A. & Martinez, C .and Weitz, D. 2008 Designer emulsions using microfluidics. *Materialstoday* **11 (4)**, 18–27.

Suryo, R. & Basaran, O.A. 2006 Tip streaming from a liquid drop forming from a tube in a co-flowing outer fluid. *Physics of Fluids* **18**, 082102.

Suryo, R., Doshi, P. & Basaran, O.A. 2006 Nonlinear dynamics and breakup of compound jets. *Physics of Fluids* **18**, 082107.

Thorsen, T., Roberts, Richard W., Arnold, Frances H. & Quake, Stephen R. 2001 Dynamic pattern formation in a vesicle-generating microfluidic device. *Phys. Rev. Lett.* **86** (18), 4163–4166.

Tomotika, S. 1935 On the instability of a cylindrical thread of a viscous liquid surrounded by another viscous fluid. *Proc. Roy. Soc.* **150**, 322–337.

Utada, A.S., Fernández-Nieves, A., Gordillo, J. M. & Weitz, D. 2008 Absolute instability of a liquid jet in a coflowing stream. *Phys. Rev. Lett.* **100**, 014502.

Utada, A.S., Fernández-Nieves, A., Stone, H.A. & Weitz, D. 2007 Dripping to jetting transitions in co-flowing liquid streams. *Phys. Rev. Lett.* **99**, 094502.

Utada, A.S., Lorenceau, E., Link, D.R., Kaplan, P.D., Stone, H.A. & Weitz, D. 2005 Monodisperse double emulsions generated from a microcapillary device. *Science.* **308**, 537–541.

Vu, T. V., Homma, S., Tryggvason, G., Wells, John C. & Takakura, H. 2013 Computations of breakup modes in laminar compound liquid jets in a coflowing fluid. *International Journal of Multiphase Flow.* **49**, 58–69.

Zarzar, D., Sresht, V., Sletten, E., Kalow, J., Blankschtein, D. & Swager, T. 2015 Dynamically reconfigurable complex emulsions via tunable interfacial tensions. *Nature* **518**, 520–524.